Controlled motility in the cyanobacterium *Trichodesmium* regulates aggregate architecture

Ulrike Pfreundt[1†], Jonasz Słomka[1†], Giulia Schneider[1], Anupam Sengupta[2], Francesco Carrara[1], Vicente Fernandez[1], Martin Ackermann[3,4], Roman Stocker[1*]

1. Institute of Environmental Engineering, Department of Civil, Environmental and Geomatic Engineering, ETH Zurich, Zurich, Switzerland
2. Physics of Living Matter, Department of Physics and Materials Science, University of Luxembourg, Luxembourg City, Grand Duchy of Luxembourg
3. Department of Environmental Systems Sciences, Microbial Systems Ecology Group, Institute of Biogeochemistry and Pollutant Dynamics, ETH Zurich, Zurich, Switzerland
4. Department of Environmental Microbiology, Eawag: Swiss Federal Institute of Aquatic Sciences, Duebendorf, Switzerland

† These authors contributed equally to this work and are listed in alphabetical order.

* Corresponding author. Email: romanstocker@ethz.ch

Abstract

A large part of the ocean's nitrogen is fixed by only few types of cyanobacteria, including *Trichodesmium*, which forms aggregates comprising hundreds of filaments arranged in organized architectures. These form upon exposure to stress and have altered ecological and biophysical characteristics compared to single filaments. Here, we report that *Trichodesmium* aggregates are active structures capable of rapidly modulating their shape, responding within minutes to changes in environmental conditions. Using video microscopy and mathematical modeling, we discovered that this reorganization is mediated by 'smart reversals' – the ability of gliding filaments to reverse direction when their overlap with other filaments diminishes. By regulating smart reversals, *Trichodesmium* filaments control aggregate architecture without central coordination. We thus propose that the modulation of gliding motility at the single filament level is an important determinant of *Trichodesmium*'s aggregation behavior and ultimately of its biogeochemical role in the ocean.

One sentence summary

Controlled motility is responsible for aggregation in the key nitrogen fixing cyanobacterium *Trichodesmium*.

Main Text

The input of new nitrogen into the ocean, and thus global primary productivity, is driven in large part by nitrogen fixation by only a few types of cyanobacteria (*1*), one of them being the genus *Trichodesmium* (*2*, *3*). Oceanographers have been puzzled by *Trichodesmium's* dual occurrence as either single multicellular filaments or aggregates comprising hundreds of filaments (*4*–*6*). Both often occur in the same water and are found in all tropical and subtropical oceanic ecosystems (*6*, *7*) and across different *Trichodesmium* species (*8*). In laboratory conditions, aggregation of *Trichodesmium* filaments typically occurs in the post-exponential growth phase (*9*–*11*). It can also be induced by depleting iron or phosphate (*12*), reducing salinity (*11*), or changing growth medium or irradiance (*13*). This suggests that aggregation is a general stress response. In comparison with filaments, aggregates perform different ecological and metabolic functions (*14*–*21*), partially due to the microbiomes they host (*22*, *23*). Aggregates create different microenvironments (*24*, *25*) that may be transiently suboxic and thus reduce nitrogen and carbon fixation compared to single filaments (*26*). However, through behaviors inaccessible to single filaments, aggregates have better access to other limiting resources. They can capture iron-loaded dust (*14*, *18*, *27*), which may help aggregates engage in iron-intense nitrogen and carbon fixation simultaneously, a hallmark of *Trichodesmium* ecology (*28*). Aggregates may be able to scavenge phosphate from depth by rapid vertical migration (*15*, *29*), and *Trichodesmium* aggregates at depths below 170 m have been observed to fix nitrogen at similar rates as aggregates in the surface ocean (*30*). Vertical migration is likely also involved in the formation of surface blooms (*31*) spanning tens of thousands of square kilometres (*32*–*34*). Yet, despite the unique ecology of *Trichodesmium* aggregates, little is known about the mechanisms by which filaments give rise to aggregates, how aggregate architecture is controlled, and on what timescale this control occurs.

Here we report that *Trichodesmium* aggregates are active filament assemblies capable of rapid structural changes in response to changes in environmental conditions and we show that this active reshaping of aggregates is realised by changes in the motility of individual filaments.

Changes in light exposure induce rapid reshaping of aggregates

We analyzed the effect of changing light conditions on aggregates of *Trichodesmium erythraeum* IMS101, a strain frequently associated with open-ocean surface blooms (*35*). Changes in light intensity are an ecologically relevant cue, occurring in the surface ocean due to cloud movement, and can induce cellular stress by generating reactive oxygen species (ROS) (*36*). We exposed naturally aggregating *T. erythraeum* cultures in late stationary growth phase to sudden changes in light intensity (light switches) (**Fig. 1**) and quantified the size and density of individual aggregates over approximately 30 h through time-lapse imaging.

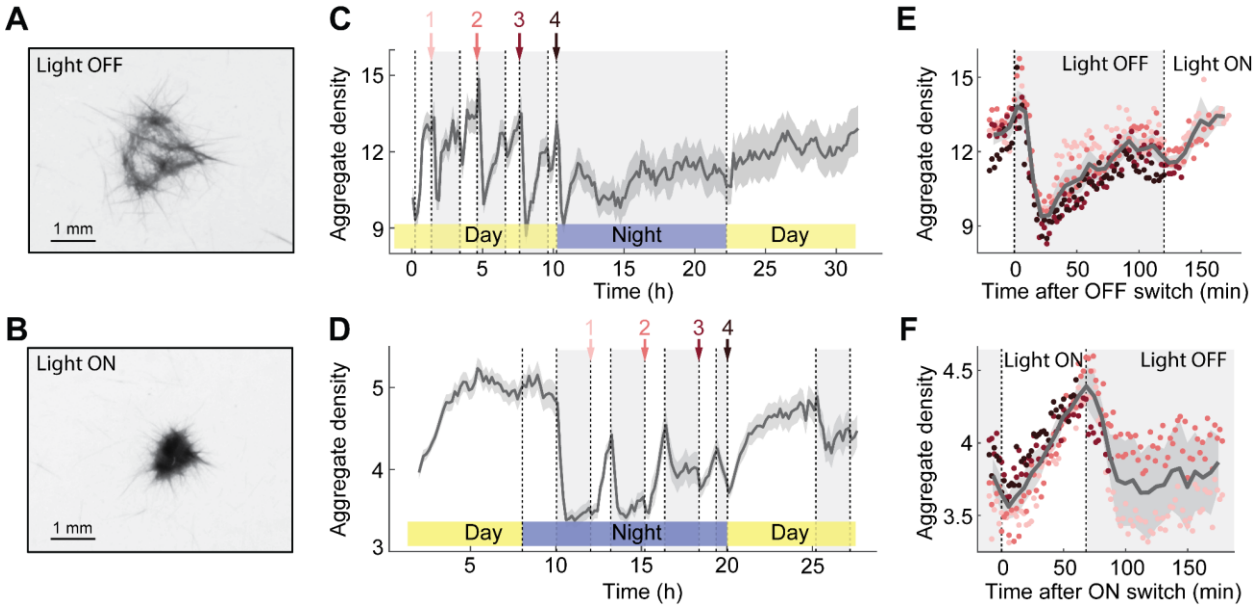

Fig . 1 | *Trichodesmium* aggregate density changes rapidly upon switches in light intensity. A, B, A puff aggregate in its loose form 15 min after a Light OFF switch (**A**) and in its dense form in 80 µmol quanta

m^{-2} s^{-1} light (**B**). **C, D,** Time series of mean aggregate density (*i.e.*, the density of filaments within aggregates, quantified as the mean pixel intensity of individual aggregates) in light-switching experiments, with four Light OFF switches (numbered arrows) during the day (**C**) and four Light ON switches (numbered arrows) during the night (**D**). Switch 4 corresponds to the normal onset of the next night/day, respectively. Light conditions were 80 µmol quanta m^{-2} s^{-1} in all cases. **E, F,** Overlays of the four Light OFF switches (**E**) from **C** and the four Light ON switches (**F**) from **D**, color-coded from pink (switch 1) to dark red (switch 4), with each data point representing the mean aggregate density of all aggregates in the imaging frame (16-19 aggregates in **E** and 26-31 aggregates in **F**). In **C-F**, aggregate density (arbitrary units) was computed as the mean pixel intensity per aggregate. Note the different scales in (**C**, **D**) and (**E**, **F**), owing to the fact that aggregate density is measured as pixel intensity, and thus not directly comparable among experiments (Materials and Methods). The grey curves show a 10-min moving average and the grey shading the 95% confidence interval of the mean.

Aggregates responded rapidly to light switches (**Movie S1, Fig. 1**). After a Light OFF switch, aggregates expanded (**Fig. 1A, B**) – the same set of filaments in the aggregate rearranged into a looser and larger aggregate – causing the average density to decrease by 33 ± 10% (mean ± sem, *n* = 18) over 24 min (**Fig. 1C, E, Movie S1**). Conversely, after a Light ON switch, aggregates tightened, causing the average density to increase by 26 ± 17% (mean ± sem, *n* = 30) over 65 min (**Fig. 1D, F, Movie S2**). The pure circadian onset of the night phase (blue horizontal bar, **Fig. 1D**), but with light kept on, did not lead to aggregate loosening. Only when the light was actually turned off the aggregates loosened (at 10 h, **Fig. 1D**). While this does not exclude circadian control of aggregation behavior, it shows that the observed responses were inducible by light changes irrespective of the time of day. Responses were rapid, starting to be visible within only 0–8 min of a switch (**Fig. 1E, F**), and were transient and reversible, i.e., aggregates returned to approximately their previous configuration after cessation of the light perturbation. A UV-

killed control culture did not form aggregates (**Movie S3**). The structural configuration of an aggregate can thus change over timescales of minutes, suggesting that active movement is implicated in aggregate loosening and tightening. These experiments also revealed that puff-like aggregates often formed sequentially: individual filaments first aggregated into tight bundles (tufts), which in turn encountered one another and rearranged into puffs (**Movie S4**). This process was also observed to occur in reverse, whereby a puff disintegrated into several tufts (**Movie S4**).

Filament–filament interactions reveal a motility mechanism to modulate aggregate shape

Trichodesmium filaments can glide on surfaces (*12*, *18*, *37*) (**Movies S5 and S6**) through an as-yet unknown locomotion mechanism. We discovered that filaments can also glide on each other, without the presence of another surface, in experiments in which we suspended a filament in liquid using a micropipette and brought a second filament into contact with it by fluid flow (**Movie S7**). Upon meeting, the two filaments started gliding against each other, without any contact to a solid surface (except the pipette tip). We next characterize the motility of individual filaments and filament pairs, and show that filament–filament gliding is an important – yet by itself not sufficient – component of aggregate reshaping.

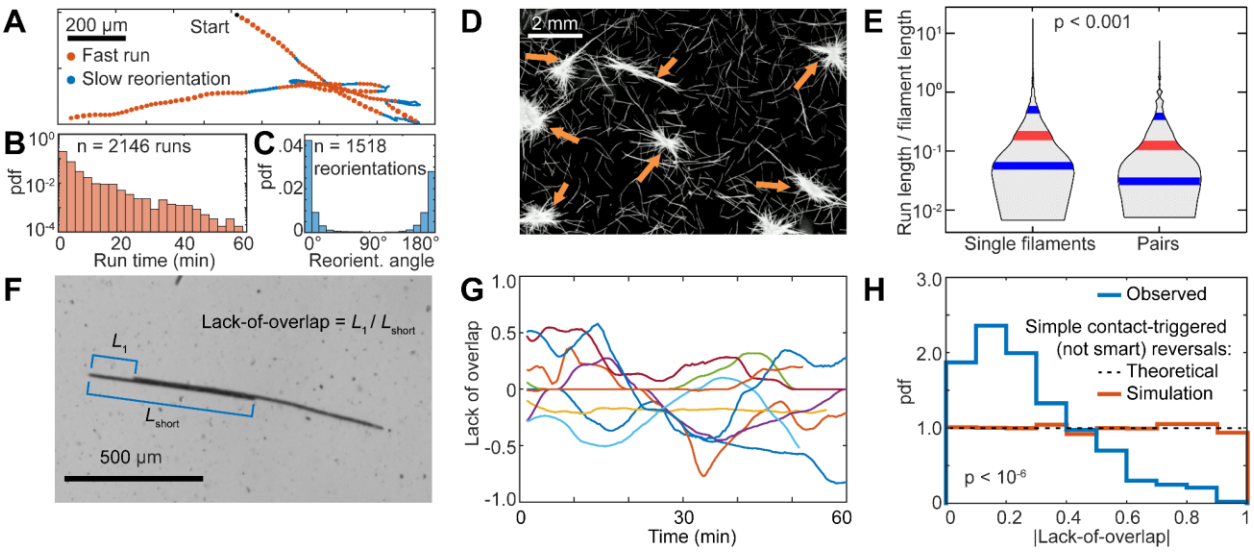

Fig. 2 | Controlled reversals characterize *Trichodesmium* aggregation. A, Trajectory of a filament gliding on a surface, segmented into runs (orange) and reorientations (blue). Dots mark the position of the centroid, with size proportional to instantaneous speed. **B,** Run times exhibit a broad distribution. **C**, Reorientation angles exhibit a nearly equal repartition between values close to 0° (continuation in the same direction) and values close to 180° (reversals). **D**, Mid-exponential *Trichodesmium* filaments exposed to menadione, which induces oxidative stress, form aggregates (orange arrows). **E**, The run length (normalized by filament length) of menadione-exposed *Trichodesmium* is markedly shorter (35% decrease in the mean) for filaments in pairs (two filaments in contact and aligned) than for single filaments [n = 12 independent experiments; $p < 0.001$, two-sample one-sided Kolmogorov–Smirnov test (n_{single} = 1964, n_{pairs} = 377)]. The grey area shows the distributions as violin plots. The red line shows the median and the blue lines show the 25th and 75th percentiles. . **F**, Filament pair illustrating the Lack-of-overlap , defined as the fraction of the shorter filament length not overlapping with the longer filament. Lack-of-overlap is positive at one end of the filament pair and negative at the other end. **G**, Lack-of-overlapas a function of time for nine filament pairs, illustrating the dynamic rearrangement between filaments. **H,** The Lack-of-overlap distribution of menadione-exposed filament pairs is strongly skewed towards small Lack-of-overlap values compared to the uniform distribution expected if filaments were

to simply increase reversal frequency upon contact ($p < 10^{-6}$, one-sample two-sided Kolmogorov–Smirnov test, $n = 53$). This is consistent with the hypothesis that *Trichodesmium* performs 'smart reversals', whereby reversals are triggered by an increase in Lack-of-overlap as filaments glide upon each other (see text).

Individual *Trichodesmium* filaments move in a series of nearly straight, fast "runs" interrupted by periods of slower motion, which we term reorientations (**Fig. 2A**). Analysing the tracks of hundreds of individual filaments (**Materials and Methods**, **Supplementary Text Section I**) on the glass surface of a microfluidic chamber (**Movie S8**), we found that filaments glide at 34.1 ± 31.9 μm min^{-1} (mean ± sd, n = 776), primarily along their long axis (**Fig. S1**). Run times exhibit a broad distribution (**Fig. 2B**) with a mean of 5.4 ± 8.2 min (mean ± sd, n = 2416). After a reorientation, filaments continue moving in the same direction or reverse, with similar probability (57 ± 1% vs. 43 ± 1%, respectively; mean ± sem, n = 1518, **Fig. 2C**). During a reversal, the leading end becomes the trailing end (**Movie S9**), as also observed previously (*12*). Gliding motility allows for fast filament movement, but filaments lacking the ability to reverse would quickly glide off a nascent aggregate. We thus inferred that reversals are key to aggregation. However, randomly occurring reversals would still cause an aggregate to disintegrate by filaments gliding off it. Consequently, we hypothesized that reversals are triggered by filament–filament contact, thereby allowing an aggregate to reshape without disintegrating.

In aggregating cultures, filaments within pairs had shorter run lengths and thus reversed more frequently than individual filaments. We induced aggregation in mid to late exponential *T. erythraeum* cultures by addition of menadione (**Fig. 2D**, **Movie S10**), which causes cellular stress via reactive oxygen species (ROS) (*38*). Menadione-induced aggregation is easier to control and thus easier to replicate than relying on post-exponential cultures, in which the exact trigger for aggregation is unknown. We analyzed

individual filaments (n = 643) and pairs of filaments that, upon encounter, aligned and glided on each other (n = 59). For both categories, we computed filament reversal frequency as well as different gliding motility statistics that might explain changes in the reversal frequency, including run time, run length, reversal probability and overall activity (i.e., the fraction of time spent in run mode) (**Table S1**). We found that filaments in pairs moved a smaller fraction of their length during a run, 35% less than single filaments (0.41 ± 0.85 vs. 0.63 ± 1.52, respectively; mean ± sd; $n_{runs,pairs}$ = 377, $n_{runs,single}$ = 1964; $p < 0.001$, two-sample one-sided Kolmogorov–Smirnov test) (**Fig. 2E**). Additionally, filaments in pairs spent more time in the run mode (**Table S1**), which induced more reorientation events. This higher activity together with shorter run lengths resulted in a reversal frequency that was nearly two-fold higher in pairs than in single filaments (0.034 ± 0.040 min^{-1} vs. 0.019 ± 0.031 min^{-1}, respectively; weighted mean ± weighted sd; n_{pairs} = 118, n_{single} = 643; weight = track length, **Supplementary Text Section II**). The fact that a filament in contact with another filament has a markedly higher reversal frequency than single filaments from the same culture suggests that filaments can respond to each other.

To understand how a filament responds to contact with another filament, we measured the 'Lack of overlap' of filament pairs. We define the Lack-of-overlap as the fraction of the shorter filament's length that is not overlapping with the longer filament (**Fig. 2F**). By tracking both filaments in a pair (n = 59 pairs, as in **Fig. 2E**), we measured their Lack-of-overlap as a function of time (**Fig. 2G**) to quantify the distribution of Lack-of-overlap values. If filaments merely increased their reversal frequency upon contact, the Lack-of-overlap would be uniformly distributed (**Fig. 2H**, **Supplementary Text Section III**). By contrast, we found that the Lack-of-overlap was strongly skewed towards small values ($p < 10^{-6}$, one-sample two-sided Kolmogorov–Smirnov test, n = 53, **Fig. 2H**). For example, instances of short filaments projecting by less than 50% of their length (|Lack-of-overlap| < 0.5) occurred nearly six times more often than filaments projecting by more than 50% (|Lack-of-overlap| > 0.5) (**Fig. 2H**). Thus, the observed increase in reversal frequency upon encounter (**Fig. 2E**) is not by itself sufficient to describe the behavior

of filaments in pairs. Rather, the prevalence of small Lack-of-overlap values suggests that reversals of filaments in pairs are not random but are informed by a sensory cue linked to filament overlap. Thus, reversals are 'smart' rather than random. We propose that this behavior is a form of thigmotaxis (*39*, *40*), the change in motility of organisms in response to contact stimuli. In the following, we refer to changes in smart reversals as thigmotaxis, as they are linked to contact between filaments, yet we highlight that the underlying molecular mechanism responsible remains unknown. Such smart reversals are a simple yet effective mechanism for filaments to remain together and rearrange upon encounter. We highlight that filament pairs in the exponentially growing control can also perform smart reversals, however, such pairs disintegrate 2.5-fold faster than in the menadione treatment, because filaments in the control perform weaker smart reversals than those treated by menadione, and furthermore because they are faster and shorter (**Supplementary Text Section IV**; **Figs. S2** and **S3**). This faster disintegration rate prevents the formation of stable aggregates in the control.

Mathematical model of smart reversals

To understand the effects on aggregation of different components of the reversal behavior of filaments, we developed an individual-based model of *Trichodesmium* that represents filaments as motile thigmotactic rods capable of sensing overlap with each other and of reversing when they detect that the overlap is decreasing (**Fig. 3**). Filaments are represented as highly elongated rods (160 μm x 8 μm), consisting of 20 cells, that can glide (speed = 32 μm min^{-1}) on surfaces and on other filaments, and adhere to each other upon contact, weakly enough to allow relative gliding (**Fig. S4, Supplementary Text Section V**). All filaments reverse randomly (rate = 32 μm min^{-1} / 160 μm = 0.2 min^{-1}) independently of cues, in line with observations that individual filaments travel approximately their length before reversing (**Fig. 2E**). Each filament monitors its overlap with filaments in contact with it, where the

overlap is defined as the number of neighboring cells on the adjacent filaments a given cell touches, averaged over the filament ('mean cell coordination number'). When a model filament senses a temporal decrease in its overlap, it reverses its gliding direction after a mean response time τ – with smaller values of τ representing greater thigmotaxis strength, i.e., a stronger tendency of filaments to stay together. Below, we vary the response timescale τ in the model to determine the effect of thigmotaxis strength on aggregation.

Our model predicts that thigmotactic filaments form organized (highly overlapping) aggregates on a surface (**Fig. 3A, Movie S11**), akin to the dynamic aggregates observed in *T. erythraeum* exposed to menadione (**Fig. 2D**, **Movie S10**). To quantify aggregation in model simulations, we compute the average overlap over all filaments in the system as a function of time (**Fig. 3B**). We focus on the three values of thigmotaxis strength, representing filaments that, after detecting a decrease in overlap (which takes approximately 10 s), (i) reverse after a short delay (τ = 0.75 s, strong thigmotaxis); (ii) reverse after an intermediate delay (τ = 12 s, medium thigmotaxis); and (iii) reverse after a long delay (τ = 75 s, weak thigmotaxis). Equivalently, for filaments in a pair moving in opposite directions and risking separation, the three model conditions of strong, intermediate, and weak thigmotaxis correspond to traveling approximately 4%, 15% and 55% of a filament length before performing a smart reversal. For strong thigmotaxis (τ = 0.75 s), smart reversals lead to the formation of tight aggregates, characterized by high overlap, by preventing filaments from escaping from aggregates: when filaments sense that their overlap with other filaments in the aggregate decreases, they rapidly trigger a reversal that on average redirects them towards the aggregate (**Fig. 3A, B**). For strong thigmotaxis, aggregation is robust against filament length variability (**Fig. S5**). Medium (τ = 12 s) or weak (τ = 75 s) thigmotaxis strengths result in looser aggregates containing fewer filaments, or almost no aggregates, respectively (**Fig. 3B**). Identifying filament pairs in these simulations shows that the response time τ controls the skewness of the Lack-of-overlap distribution (**Fig. 3C)**, thus linking the response time τ – a core model parameter characterizing

smart reversals – with the Lack-of-overlap distribution observed in experiments (**Fig. 2H**). When τ is small (strong thigmotaxis), the Lack-of-overlap is skewed towards small values (**Fig. 3C)**, in line with our observations (**Fig. 2H**). Because τ increases (medium and weak thigmotaxis), the Lack-of-overlap distribution becomes more uniform (**Fig. 3C)**.

The response timescale τ can be approximately measured in our experiments from the rate of disintegration of filament pairs (**Supplementary Text Section VI**). These measurements indicate that filaments in menadione correspond to medium-to-strong thigmotaxis in the model, whereas filaments in the control correspond to weak-to-medium thigmotaxis in the model (**Fig. S5**). Additionally, our data show that slower or longer filaments perform stronger thigmotaxis than faster or shorter ones, respectively (**Supplementary Text Section VII, Table S2**).

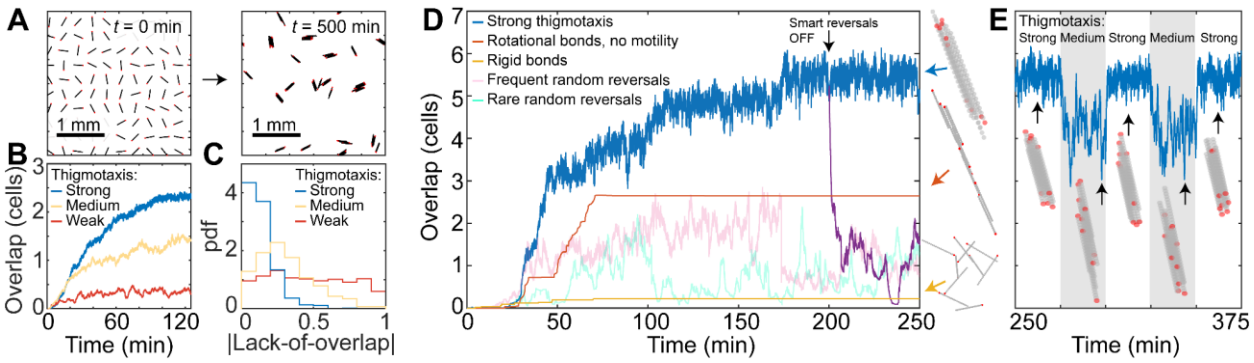

Fig. 3 | Organized aggregate architecture in 3D emerges from smart reversals. A, In our 2D model of aggregation on a surface, filaments performing smart reversals (τ = 0.75 s, *n* = 100), initially separated and oriented randomly on the surface, form aggregates of oscillating filaments (**Movie S11**), akin to those observed experimentally (**Fig. 2D**). **B**, The time course of filament overlap (mean cell coordination number) on a surface for filaments performing smart reversals with different response times (τ = 0.75 s, blue; τ = 12 s, yellow; τ = 75 s, red) shows that tuning the response time directly controls the strength of

thigmotaxis – small values of τ realize strong thigmotaxis characterized by the emergence of highly overlapping aggregates. Displayed are averages over 6 runs for simulations with 20 filaments. **C**, Distribution of the Lack-of-overlap of filament pairs identified in 2D simulations (at least $n = 6$) for different thigmotaxis strengths, showing that thigmotaxis skews the Lack-of-overlap towards small values, consistent with the experimental observations (**Fig. 2H**). **D**, Overlap as a function of time predicted by 3D simulations of 10 filaments in suspension. Aggregates form from an initial seed filament that collects other filaments by random encounters . The effect of three possible mechanisms following filament encounter is shown: (i) filaments form rigid bonds and do not rearrange, which creates fractal-like aggregates (yellow); (ii) filaments are not motile and align under external torques (e.g., turbulence-induced), which creates elongated chains (red); or (iii) motile filaments perform smart reversals with strong thigmotaxis ($\tau = 0.75$ s), which creates compact aggregates (blue). Switching off smart reversals (while retaining random reversals) leads to rapid disintegration of aggregates (purple). Finally, random reversals do not create stable aggregates (pink and cyan). **E,** Continuation of the model simulation for the aggregate of filaments executing strong thigmotaxis [blue curve in panel (**D**)], when the thigmotaxis strength is modulated between strong ($\tau = 0.75$ s) and medium ($\tau = 12$ s). The resulting tightening and loosening of the aggregate reproduces the response of aggregates exposed to light switches (**Fig. 1**).

We also modeled aggregate formation in 3D to show that smart reversals are key to the formation of organized aggregates in a liquid suspension (i.e., away from solid surfaces), like the marine habitat of *Trichodesmium*. This model represents sequential random arrivals of randomly oriented filaments onto a single seed filament, with which they align upon encounter (**Fig. 3D)**, mimicking, for example, encounters and alignment driven by ocean turbulence (**Fig. S6**, **Supplementary Text Sections VIII and IX**). We find that strong thigmotaxis converts successive random encounters into an organized aggregate

characterized by large overlap (blue curve in **Fig. 3D, Movie S12**). Such large overlap (> 5), which approaches values characterizing random packing of spheres (*41*), indicates that a random cell within the aggregate has typically five or more neighboring cells, not including cells on the same filament. Importantly, switching off smart reversals after an organized aggregate has formed (thus leaving only random reversals) leads to rapid disintegration of the aggregate (purple curve in **Fig. 3D)**. Similarly, random reversals alone do not lead to stable aggregates, with filaments only forming small, transient aggregates that continuously disintegrate [for both high (2 min^{-1}) and low (0.4 min^{-1}) rates of random reversals, pink and cyan in **Fig. 3D**]. Additionally, simple adhesion upon encounter, without rearrangement, would result in fractal aggregate morphologies (*42*) (yellow curve in **Fig. 3D**, **Movie S13**). Lastly, if filaments stuck to each other and aligned in flow, but were otherwise non-motile, they would form elongated chains (red curve in **Fig. 3D**, **Movie S14**). Both fractals and chains could emerge in scenarios where filaments were non-motile and sticky. Only strong thigmotaxis produces organized aggregates characterized by large overlap (approximately 5 to 6), whereas all other mechanisms considered above resulted in values of overlap at least 50% smaller.

Smart reversals can also explain the rapid, dynamic tightening and loosening of aggregates that we observed upon switches in light intensity (**Fig. 1)**. Modeling the response to an increase and decrease in light intensity as strong and medium thigmotaxis, respectively, reproduces the observed tightening and loosening of aggregates (**Fig. 3E**). Specifically, the loosening of a compact model aggregate by approximately 30% (measured as the change in overlap in the model; **Fig. 3E, Movie S15**) is akin to the change in aggregate density (a proxy for total overlap) observed experimentally (**Fig. 1, Movie S16).** Thus, a change in single-filament behavior – modeled as a change in the response time τ between detecting a decrease in overlap and reversing – can explain the rapid reshaping of aggregates in response to light switches.

296 Smart reversals represent an effective mechanism for filaments to remain together after an encounter.
297 These encounters occur differently on a surface and in the ocean. On a surface, such as in most of our
298 experiments, gliding can drive encounters, which occur on the timescale of an hour (**Fig. S3E**). In
299 contrast, in the three-dimensional water column without surfaces to glide on, encounters are most likely
300 driven by turbulence and buoyancy. The typical encounter timescale between buoyant (density offset 50
301 kg m^{-3}) individual filaments is below twenty hours (*43*) for a turbulent intensity characteristic of the
302 ocean surface layer (10^{-6} W kg^{-1}) at an organism concentration representing bloom conditions (10^{7}
303 filaments m^{-3}) (*44*). Consequently, the encounter timescale in the ocean is short enough to convert
304 individual filaments into aggregates within several days, even at tenfold lower concentrations, as we
305 demonstrated using a coagulation model that accounts for aggregate-aggregate encounters (**Fig. S7**,
306 **Supplementary Text Section X**). By contrast, because *Trichodesmium*'s doubling time is a few days (*45*–
307 *47*), it would take several weeks for a single filament to grow into a sizeable aggregate, suggesting that
308 encounters are likely more important than growth in driving the formation of aggregates. Still, an
309 encounter timescale of many hours is much longer than the tens of minutes required for a filament to
310 travel its length. Smart reversals protect the nascent aggregate from disintegrating: if filaments lose
311 each other, it takes hours before a new filament is encountered. Additionally, turbulence in the ocean
312 surface layer is unlikely to separate a pair of filaments that stick to each other, because it exerts shear
313 forces on the order of tens of picoNewtons (**Supplementary Text Section X**), much smaller than filament
314 adhesive forces, likely mediated by cellular appendages, which are in the range of tens of nanoNewtons
315 (*12*).

316

317

318

Discussion

In our experiments, puff-like aggregates often formed by merging tufts and tufts could form from disintegrating puffs (**Movie S4**). This sequential formation of puffs is corroborated by dilution experiments, in which only tufts formed (**Fig. S8**). In the ocean, *Trichodesmium* filaments are dilute (10^4–10^6 m^{-3}) (*3*, *6*), separated from each other by many filament lengths, corresponding to the conditions of our model of aggregate formation in 3D: puffs may then emerge from encounters between tufts. Puffs may also form through other mechanisms (e.g., aggregation on dust particles (*14*, *48*)) and some strains may only form puffs or tufts (*8*, *23*). Our work, however, indicates that these two morphologies are less static than currently assumed and can reshape into one another. This might be broadly applicable, since most *Trichodesmium* clades (except Clade IV) occur as both tufts and puffs (*23*). *Trichodesmium* aggregates can comprise different clades (*23*), corroborating the idea of encounter-driven aggregation. Whether clades can tune smart reversals to avoid other strains, such as non-diazotrophic species (*49*), and thus manipulate aggregate composition, remains an open question.

Aggregates have been suggested to form through increased stickiness, mediated by appendages (*12*) or exopolymers (*50*). However, our model shows that adhesion alone does not lead to organized aggregates. While a role for motility in aggregation has been suggested (*12*, *18*, *37*), uncoordinated motility would lead to aggregate disintegration and cannot account for reversible aggregate tightening and loosening. Our experiments instead indicate that *T. erythraeum* adjusts its motility in response to a sensory cue, related to the overlap with other filaments. We propose that this response is triggered by surface contact, like C-signaling in myxobacteria (*51*). We find that intra-filament cell–cell autoinduction could plausibly trigger reversals (**Fig. S9**), yet more work is needed to unravel molecular mechanisms.

Our work suggests that smart reversals allow *Trichodesmium* to react to environmental changes as transient as shifting cloud cover. Aggregates may loosen to gain exposure to light or tighten to self-

shade. The transient response we observed suggests that it represents the initial, fastest adaptation to environmental changes, ahead of more drastic adaptations (e.g., proteomic reorganization). The rapid changes to aggregate density also modulate the cells' and their microbiome's exposure to gases and chemicals, which may allow them to tune metabolic processes and vertical migration.

Trichodesmium aggregation through motility is an example of an active matter system (*52*, *53*). It bears analogies with the formation of fruiting bodies in *Myxococcus xanthus*, resulting from jamming driven by high cell densities, gliding and reversals (*54*), and with the behavior of *Pseudomonas aeruginosa*, which avoids jamming by reversing upon contact (*55*). *Trichodesmium* aggregation is however different, as its concentration in the ocean is too low for jamming (**Supplementary Text Section XI**). Instead, *Trichodesmium* uses smart reversals to convert encounters into aggregates. Aggregation also occurs in other filamentous cyanobacteria (e.g, *Oscillatoria terebriformis* (*56*), *Nostoc punctiforme* (*57*, *58*)) and in multispecies freshwater cyanospheres (*59*, *60*), but in all cases aggregation mechanisms remain unclear.

Previous work showed that *Trichodesmium* filaments can wiggle to convey captured iron particles to the core of their aggregate (*14*, *18*, *27*). We showed that filament behavior further controls the aggregate's structure itself (**Fig. S10**). Ultimately, thus, the biogeochemical importance of *Trichodesmium* – as a nitrogen fixer, primary producer and vector of CO_2 sequestration to depth – hinges on the decentralized yet coordinated behavior of individual filaments.

References

1. C. Martínez-Pérez, W. Mohr, C. R. Löscher, J. Dekaezemacker, S. Littmann, P. Yilmaz, N. Lehnen, B. M. Fuchs, G. Lavik, R. A. Schmitz, J. LaRoche, M. M. M. Kuypers, The small unicellular diazotrophic symbiont, UCYN-A, is a key player in the marine nitrogen cycle. *Nat. Microbiol*. **1**, 1–7 (2016).

2. E. J. Carpenter, D. G. Capone, "Nitrogen fixation in the marine environment" in *Nitrogen In The Marine Environment* (Elsevier, San Diego, ed. 2, 2008), pp. 141–198.

3. R. M. Letelier, D. M. Karl, Role of *Trichodesmium* spp. in the productivity of the subtropical North Pacific Ocean. *Mar. Ecol. Prog. Ser*. **133**, 263–273 (1996).

4. M. Rodier, R. Le Borgne, Population and trophic dynamics of *Trichodesmium thiebautii* in the SE lagoon of New Caledonia. Comparison with *T. erythraeum* in the SW lagoon. *Mar. Pollut. Bull.* **61**, 349–359 (2010).

5. I. Bryceson, P. Fay, Nitrogen fixation in *Oscillatoria* (*Trichodesmium*) *erythraea* in relation to bundle formation and trichome differentiation. *Mar. Biol.* **61**, 159–166 (1981).

6. E. J. Carpenter, A. Subramaniam, D. G. Capone, Biomass and primary productivity of the cyanobacterium *Trichodesmium* spp. in the tropical N Atlantic Ocean. *Deep Sea Res. Part I Oceanogr. Res. Pap.* **51**, 173–203 (2004).

7. C. S. Davis, D. J. McGillicuddy, Transatlantic abundance of the N_2-fixing colonial cyanobacterium *Trichodesmium*. *Science*. **312**, 1517–1520 (2006).

8. A. M. Hynes, E. A. Webb, S. C. Doney, J. B. Waterbury, Comparison of cultured *Trichodesmium* (Cyanophyceae) with species characterized from the field. *J. Phycol*. **48**, 196–210 (2012).

9. P. R. F. Bell, P. J. R. Uwins, I. Elmetri, J. A. Phillips, F.-X. Fu, A. J. E. Yago, Laboratory culture studies of *Trichodesmium* isolated from the Great Barrier Reef Lagoon, Australia. *Hydrobiologia*. **532**, 9–21 (2005).

10. L. Prufert-Bebout, H. W. Paerl, C. Lassen, Growth, nitrogen fixation, and spectral attenuation in cultivated *Trichodesmium* species. *Appl. Environ. Microb.* **59**, 1367–1375 (1993).

11. Fei-Xue Fu, P. R. F. Bell, Effect of salinity on growth, pigmentation, N2 fixation and alkaline phosphatase activity of cultured *Trichodesmium* sp. *Mar. Ecol. Prog. Ser*. **257**, 69–76 (2003).

12. Y. Tzubari, L. Magnezi, A. Be'er, I. Berman-Frank, Iron and phosphorus deprivation induce sociality in the marine bloom-forming cyanobacterium *Trichodesmium*. *ISME J.* **12**, 1682–1693 (2018).

13. Y.-B. Chen, J. P. Zehr, M. Mellon, Growth and nitrogen fixation of the diazotrophic filamentous nonheterocystous cyanobacterium *Trichodesmium* sp. IMS 101 in defined media: Evidence for a circadian rhythm. *J. Phycol*. **32**, 916–923 (1996).

14. M. Rubin, I. Berman-Frank, Y. Shaked, Dust- and mineral-iron utilization by the marine dinitrogen-fixer *Trichodesmium*. *Nat. Geosci.* **4**, 529–534 (2011).

15. A. E. White, Y. H. Spitz, R. M. Letelier, Modeling carbohydrate ballasting by *Trichodesmium* spp. *Mar. Ecol. Prog. Ser.* ***323***, 35–45 (2006).

16. K. R. Frischkorn, M. Rouco, B. A. S. Van Mooy, S. T. Dyhrman, Epibionts dominate metabolic functional potential of *Trichodesmium* colonies from the oligotrophic ocean. *ISME J.* **11**, 2090–2101 (2017).

17. K. R. Frischkorn, S. T. Haley, S. T. Dyhrman, Coordinated gene expression between *Trichodesmium* and its microbiome over day–night cycles in the North Pacific Subtropical Gyre. *ISME J.* **12**, 997–1007 (2018).

18. J. G. Rueter, D. A. Hutchins, R. W. Smith, N. L. Unsworth, "Iron nutrition of *Trichodesmium*" in *Marine Pelagic Cyanobacteria: Trichodesmium and other Diazotrophs*, E. J. Carpenter, D. G. Capone, J. G. Rueter, Eds. (Springer Netherlands, 1992), pp. 289–306.

19. K. R. Frischkorn, S. T. Haley, S. T. Dyhrman, Transcriptional and proteomic choreography under phosphorus deficiency and re-supply in the N_2 fixing cyanobacterium *Trichodesmium erythraeum*. *Front. Microbiol.* **10**, 00330 (2019).

20. M. D. Lee, N. G. Walworth, E. L. McParland, F.-X. Fu, T. J. Mincer, N. M. Levine, D. A. Hutchins, E. A. Webb, The *Trichodesmium* consortium: conserved heterotrophic co-occurrence and genomic signatures of potential interactions. *ISME J.* **11**, 1813–1824 (2017).

21. B. A. S. Van Mooy, L. R. Hmelo, L. E. Sofen, S. R. Campagna, A. L. May, S. T. Dyhrman, A. Heithoff, E. A. Webb, L. Momper, T. J. Mincer, Quorum sensing control of phosphorus acquisition in *Trichodesmium* consortia. *ISME J*. **6**, 422–429 (2012).

22. S. Basu, M. Gledhill, D. de Beer, S. G. Prabhu Matondkar, Y. Shaked, Colonies of marine cyanobacteria *Trichodesmium* interact with associated bacteria to acquire iron from dust. *Communications Biol*. **2**, 284 (2019).

23. M. Rouco, S. T. Haley, S. T. Dyhrman, Microbial diversity within the *Trichodesmium* holobiont. *Environ. Microbiol.* **18**, 5151–5160 (2016).

24. M. Eichner, S. Basu, M. Gledhill, D. de Beer, Y. Shaked, Hydrogen dynamics in *Trichodesmium* colonies and their potential role in mineral iron acquisition. *Front. Microbiol.* **10**, 01565 (2019).

25. M. J. Eichner, I. Klawonn, S. T. Wilson, S. Littmann, M. J. Whitehouse, M. J. Church, M. M. Kuypers, D. M. Karl, H. Ploug, Chemical microenvironments and single-cell carbon and nitrogen uptake in field-collected colonies of *Trichodesmium* under different pCO_2. *ISME J.* **11**, 1305–1317 (2017).

26. M. Eichner, S. Thoms, B. Rost, W. Mohr, S. Ahmerkamp, H. Ploug, M. M. M. Kuypers, D. Beer, N_2 fixation in free-floating filaments of *Trichodesmium* is higher than in transiently suboxic colony microenvironments. *New Phytol*. **222**, 852–863 (2019).

27. N. Kessler, R. Armoza-Zvuloni, S. Wang, S. Basu, P. K. Weber, R. K. Stuart, Y. Shaked, Selective collection of iron-rich dust particles by natural *Trichodesmium* colonies. *ISME J.* **14**, 91–103 (2019).

28. N. A. Held, J. B. Waterbury, E. A. Webb, R. M. Kellogg, M. R. McIlvin, M. Jakuba, F. W. Valois, D. M. Moran, K. M. Sutherland, M. A. Saito, Dynamic diel proteome and daytime nitrogenase activity supports buoyancy in the cyanobacterium *Trichodesmium*. *Nat. Microbiol*. **7**, 300–311 (2022).

29. T. A. Villareal, E. J. Carpenter, Buoyancy regulation and the potential for vertical migration in the oceanic cyanobacterium *Trichodesmium*. *Microb. Ecol.* **45**, 1–10 (2003).

30. M. Benavides, S. Bonnet, F. A. C. Le Moigne, G. Armin, K. Inomura, S. Hallstrøm, L. Riemann, I. Berman-Frank, E. Poletti, M. Garel, O. Grosso, K. Leblanc, C. Guigue, M. Tedetti, C. Dupouy, Sinking *Trichodesmium* fixes nitrogen in the dark ocean. *ISME J*. **16**, 2398–2405 (2022).

31. M. Rodier, R. Le Borgne, Population dynamics and environmental conditions affecting *Trichodesmium* spp. (filamentous cyanobacteria) blooms in the south–west lagoon of New Caledonia. *J. Exp. Mar. Biol. Ecol*. **358**, 20–32 (2008).

32. D. G. Capone, A. Subramaniam, J. P. Montoya, M. Voss, C. Humborg, A. M. Johansen, R. L. Siefert, E. J. Carpenter, An extensive bloom of the N_2-fixing cyanobacterium *Trichodesmium erythraeum* in the central Arabian Sea. *Mar. Ecol. Prog. Ser*. **172**, 281–292 (1998).

33. D. M. Karl, R. Letelier, D. V. Hebel, D. F. Bird, C. D. Winn, "*Trichodesmium* blooms and new nitrogen in the North Pacific Gyre" in *Marine Pelagic Cyanobacteria: Trichodesmium and other Diazotrophs*, E. J. Carpenter, D. G. Capone, J. G. Rueter, Eds. (Springer Netherlands, 1992), pp. 219–237.

34. E. J. Carpenter, D. G. Capone, "Nitrogen fixation in *Trichodesmium* blooms" in *Marine Pelagic Cyanobacteria: Trichodesmium and other Diazotrophs*, E. J. Carpenter, D. G. Capone, J. G. Rueter, Eds. (Springer Netherlands, 1992), pp. 211–217.

35. K. M. Orcutt, U. Rasmussen, E. A. Webb, J. B. Waterbury, K. Gundersen, B. Bergman, Characterization of *Trichodesmium* spp. by genetic techniques. *Appl. Environ. Microbiol*. **68**, 2236–2245 (2002).

36. N. Blot, D. Mella-Flores, C. Six, G. Le Corguillé, C. Boutte, A. Peyrat, A. Monnier, M. Ratin, P. Gourvil, D. A. Campbell, L. Garczarek, Light history influences the response of the marine cyanobacterium *Synechococcus* sp. WH7803 to oxidative stress. *Plant Physiol.* **156**, 1934–1954 (2011).

37. H. W. Paerl, B. M. Bebout, "Oxygen dynamics in *Trichodesmium* spp. aggregates" in *Marine Pelagic Cyanobacteria: Trichodesmium and other Diazotrophs*, E. J. Carpenter, D. G. Capone, J. G. Rueter, Eds. (Springer Netherlands, 1992), pp. 43–59.

38. X. Kammerscheit, F. Chauvat, C. Cassier-Chauvat, First *in vivo* evidence that glutathione-S-transferase operates in photo-oxidative stress in cyanobacteria. *Front. Microbiol.* **10**, 01899 (2019).

39. S. J. Schnörr, P. J. Steenbergen, M. K. Richardson, D. L. Champagne, Measuring thigmotaxis in larval zebrafish. *Behav. Brain Res.* **228**, 367–374 (2012).

40. J. Sikora, Z. Baranowski, M. Zajaczkowska, Two-state model of *Paramecium bursaria* thigmotaxis. *Experientia*. **48**, 789–792 (1992).

41. L. V. Migal, V. G. Bondarev, N. A. Chekanov, T. P. Bondareva, Simulation of the coordination number of random sphere packing. *J. Phys. Conf. Ser.* **1479**, 012097 (2020).

42. J. R. Rothenbuhler, J.-R. Huang, B. A. DiDonna, A. J. Levine, T. G. Mason, Mesoscale structure of diffusion-limited aggregates of colloidal rods and disks. *Soft Matter*. **5**, 3639–3645 (2009).

43. J.-A. Arguedas-Leiva, J. Słomka, C. C. Lalescu, R. Stocker, M. Wilczek, Elongation enhances encounter rates between phytoplankton in turbulence. *P. Natl. Acad. Sci. USA.* **119**, e2203191119 (2022).

44. W. M. Dunstan, J. Hosford, The distribution of planktonic blue green algae related to the hydrography of the Georgia Bight. *Bullet. Mar. Sci.* **27**, 824–829 (1977).

45. E. Breitbarth, J. Wohlers, J. Kläs, J. LaRoche, I. Peeken, Nitrogen fixation and growth rates of *Trichodesmium* IMS-101 as a function of light intensity. *Mar. Ecol. Prog. Ser.* **359**, 25–36 (2008).

46. C. M. Holl, J. P. Montoya, Diazotrophic growth of the marine cyanobacterium *Trichodesmium* IMS101 in continuous culture: effects of growth rate on N_2-fixation rate, biomass, and C:N:P stoichiometry. *J. Phycol.* **44**, 929–937 (2008).

47. M. R. Mulholland, D. G. Capone, Nitrogen fixation, uptake and metabolism in natural and cultured populations of *Trichodesmium* spp. *Mar. Ecol. Prog. Ser*. **188**, 33–49 (1999).

48. N. A. Held, K. M. Sutherland, E. A. Webb, M. R. McIlvin, N. R. Cohen, A. J. Devaux, D. A. Hutchins, J. B. Waterbury, C. M. Hansel, M. A. Saito, Mechanisms and heterogeneity of in situ mineral processing by the marine nitrogen fixer *Trichodesmium* revealed by single-colony metaproteomics. *ISME Commun.* **1**, 35 (2021).

49. T. O. Delmont, Discovery of nondiazotrophic *Trichodesmium* species abundant and widespread in the open ocean. *P. Natl. Acad. Sci. USA*. **118**, e2112355118 (2021).

50. I. Berman-Frank, G. Rosenberg, O. Levitan, L. Haramaty, X. Mari, Coupling between autocatalytic cell death and transparent exopolymeric particle production in the marine cyanobacterium *Trichodesmium*. *Environ. Microbiol*. **9**, 1415–1422 (2007).

51. D. Kaiser, Signaling in myxobacteria. *Annu. Rev. Microbiol.* **58**, 75–98 (2004).

52. M. Bär, R. Großmann, S. Heidenreich, F. Peruani, Self-propelled rods: insights and perspectives for active matter. *Annu. Rev. Condens. Matter Phys.* **11**, 441–466 (2020).

53. M. C. Marchetti, J. F. Joanny, S. Ramaswamy, T. B. Liverpool, J. Prost, M. Rao, R. A. Simha, Hydrodynamics of soft active matter. *Rev. Mod. Phys.* **85**, 1143–1189 (2013).

54. G. Liu, A. Patch, F. Bahar, D. Yllanes, R. D. Welch, M. C. Marchetti, S. Thutupalli, J. W. Shaevitz, Self-driven phase transitions drive *Myxococcus xanthus* fruiting body formation. *Phys. Rev. Lett.* **122**, 248102 (2019).

55. M. J. Kühn, L. Talà, Y. F. Inclan, R. Patino, X. Pierrat, I. Vos, Z. Al-Mayyah, H. Macmillan, J. Negrete, J. N. Engel, A. Persat, Mechanotaxis directs *Pseudomonas aeruginosa* twitching motility. *P. Natl. Acad. Sci. USA*. **118**, e2101759118 (2021).

56. R. W. Castenholz, Aggregation in a thermophilic *Oscillatoria*. *Nature*. **215**, 1285 (1967).

57. A. Wilde, C. W. Mullineaux, Motility in cyanobacteria: polysaccharide tracks and Type IV pilus motors. *Mol. Microbiol.* **98**, 998–1001 (2015).

58. A. Guljamow, M. Kreische, K. Ishida, A. Liaimer, B. Altermark, L. Bähr, C. Hertweck, R. Ehwald, E. Dittmann, High-density cultivation of terrestrial nostoc strains leads to reprogramming of secondary metabolome. *Appl. Environ. Microb.* **83**, e01510-17 (2017).

59. K. Milferstedt, W. C. Kuo-Dahab, C. S. Butler, J. Hamelin, A. S. Abouhend, K. Stauch-White, A. McNair, C. Watt, B. I. Carbajal-González, S. Dolan, C. Park, The importance of filamentous cyanobacteria in the development of oxygenic photogranules. *Sci. Rep*. **7**, 17944 (2017).

60. S. J. N. Duxbury, S. Raguideau, J. Rosko, K. Cremin, M. Coates, C. Quince, O. S. Soyer, Reproducible spatial structure formation and stable community composition in the cyanosphere predicts metabolic interactions. bioRxiv 2022.12.13.520286 [Preprint] (2022). https://doi.org/10.1101/2022.12.13.520286.

Additional references in Materials and Methods:

61. D. Polyviou, A. Hitchcock, A. J. Baylay, C. M. Moore, T. S. Bibby. Phosphite utilization by the globally important marine diazotroph *Trichodesmium*. *Environ. Microbiol. Rep.* **7**, 824–830 (2015).

62. R. E. Isele-Holder, J. Elgeti, G. Gompper, G. Self-propelled worm-like filaments: spontaneous spiral formation, structure, and dynamics. *Soft Matter* **11**, 7181–7190 (2015).

63. T. Kiørboe, *A Mechanistic Approach to Plankton Ecology*. (Princeton University Press, 2018).

64. M. V. Smoluchowski, Drei Vortrage uber Diffusion, Brownsche Bewegung und Koagulation von Kolloidteilchen. *Zeitschrift fur Physik* **17**, 557–585 (1916).

65. J. Słomka, R. Stocker, On the collision of rods in a quiescent fluid. *P. Natl. Acad. Sci. USA.* **117**, 3372–3374 (2020).

66. J. Słomka, R. Stocker. Bursts Characterize Coagulation of Rods in a Quiescent Fluid. *Phys. Rev. Lett.* **124**, 258001 (2020).

67. P.G. Saffman, J. S. Turner, On the collision of drops in turbulent clouds. *J. Fluid. Mech.* **1**, 16–30 (1956).

Additional references in Supplementary Text:

68. G. Bradski, The openCV library. *Dr Dobb's J. Software Tools* **25**, 120–123 (2000).

69. I. F. Sbalzarini, P. Koumoutsakos, Feature point tracking and trajectory analysis for video imaging in cell biology. *J. Struct. Biol.* **151**, 182–195 (2005).

70. K. Jaqaman, D. Loerke, M. Mettlen, H. Kuwata, S. Grinstein, S. L. Schmid, G. Danuser, Robust single-particle tracking in live-cell time-lapse sequences. *Nat. Methods* **5**, 695–702 (2008).

71. R. E. Goldstein, Point of View: Are theoretical results 'Results'? *Elife* **7**, e40018 (2018).

72. D. A. Weitz, M. Oliveria, Fractal structures formed by kinetic aggregation of aqueous gold colloids. *Phys. Rev. Lett.* **52**, 1433 (1984).

73. J. Wang, J. Zhou, G. P. Donaldson, S. Nakayama, L. Yan, Y. F. Lam, V. T. Lee, H. O. Sintim, Conservative change to the phosphate moiety of cyclic diguanylic monophosphate remarkably affects its polymorphism and ability to bind DGC, PDE, and PilZ proteins. *J. Am. Chem. Soc.* **133**, 9320–9330 (2011).

74. K. Makuch, R. Ho\lyst, T. Kalwarczyk, P. Garstecki, J. F. Brady, Diffusion and flow in complex liquids. *Soft Matter* **16**, 114–124 (2020).

75. G. B. Jeffery, The motion of ellipsoidal particles immersed in a viscous fluid. *Proc. R. Soc. Lond. A Mat.* **102**, 161–179 (1922).

76. M. E. Cates, J. Tailleur, Motility-induced phase separation. *Annu. Rev. Condens. Matter Phys.* **6**, 219–244 (2015).

Acknowledgements: We thank Wolfgang Hess for *Trichodesmium* cultures, Ewelina Borowiecka for help with the figures, and Russell Naisbit, Uria Alcolombri and Johannes Keegstra for discussions.

Funding: We gratefully acknowledge funding from an ETH Zurich Postdoctoral Fellowship to U. P.; from an ETH Zurich Postdoctoral Fellowship and a Swiss National Science Foundation Ambizione Grant (No. PZ00P2_202188) to J.S.; from the ATTRACT Investigator Grant (No. A17/MS/11572821/MBRACE) and FNR-CORE Grant (No. C19/MS/13719464/TOPOFLUME/Sengupta) from the Luxembourg National Research Fund. to A. S.; from the Simons Foundation through the Principles of Microbial Ecosystems (PriME) collaboration (grant 542389 and 542395) to M. A.; from a Gordon and Betty Moore Foundation Symbiosis in Aquatic Systems Investigator Award (GBMF9197), the Simons Foundation through the Principles of Microbial Ecosystems (PriME) collaboration (grant 542395) and the Swiss National Science Foundation, National Centre of Competence in Research (NCCR) Microbiomes (No. 51NF40_180575) to R. S.

Author contributions: U. P., J. S., A. S., M. A. and R. S. designed research. U. P. and G. S. conducted experiments. J. S. developed mathematical models. U. P., G. S., J. S. and R. S. analyzed data. A. S. provided support with initial experiments and preliminary data analyzes. U. P., J. S., M. A. and R. S wrote the paper.

Competing interests: The authors declare no competing interests.

Data and materials availability: Data that support the findings of this study are available from the ETH Research Collection (DOI: 10.3929/ethz-b-000596515).

Supplementary Material: Supplementary Materials for this study includes Materials and Methods, Supplementary Text, Supplementary Figures (Figs. S1 to S13), Supplementary Tables (Tables S1 to S3) and Movies (Movies S1 to S16).

Science
AAAS

Supplementary Materials for

Controlled motility in the cyanobacterium *Trichodesmium* regulates aggregate architecture

Ulrike Pfreundt, Jonasz Słomka, Giulia Schneider, Anupam Sengupta, Francesco Carrara, Vicente I. Fernandez, Martin Ackermann, Roman Stocker
Correspondence to: romanstocker@ethz.ch

This PDF file includes:

Other Supplementary Materials for this manuscript include the following:

Materials and Methods

Culture of *Trichodesmium erythraeum*

Trichodesmium erythraeum IMS 101 cultures were obtained from Wolfgang Hess, University of Freiburg. Cultures were grown in 25 cm^2 cell culture flasks (Nunc EasYFlask, Thermo Scientific) in YBCII medium (*13*) with modified trace metals (*61*) (cultures used under the Ecogen/Bafu permit; case number A161698). Cultures were maintained in a phytochamber (AlgaeTron AG230, Photon Systems Instruments) at 25 °C and a 12 h:12 h light:dark cycle under white cool LED light (65–85 µmol quanta m^{-2} s^{-1} from above, depending on the exact positioning of the light meter, on a rotational shaker (Heidolph Unimax 1010) at 160 rpm. The doubling time of cultures in this setup was about 3 d, as quantified once by measuring the increase of cumulative filament length per volume over time using a Sedgewick Rafter counting chamber. Every 14 days, before the end of the exponential growth phase, cultures were diluted 1:25 with fresh YBCII medium in a new flask. Older, undiluted cultures were kept for experiments with post-exponential cultures (used to produce the data for Fig. 1), which were performed after such a culture started visually aggregating (usually around three weeks after the last dilution). The growth curve was not obtained anew for each experiment. For all other experiments, an exponentially growing culture 14 days after the last dilution was briefly removed from the phytochamber, split into control and experimental samples in two new flasks, and 5 µM menadione (2-methylnaphthalene-1,4-dione, final concentration) added to the experimental sample to induce aggregation. Both samples were then returned to the phytochamber on the shaker for ~1 h, before the start of experiments. All experiments were performed in temperature-controlled environments at 25 °C.

Experimental setups

Imaging chamber. For observation and quantification of the behavior of large *Trichodesmium* aggregates, we built a custom imaging chamber that consisted of an opaque chamber (80 × 40 × 80 cm, L × W × H, with access provided by two doors on one side) that housed the sample, the imaging setup, and a temperature-controlled ventilation system. Images were obtained using a Canon EOS 80D camera with a fixed focal length objective (Canon EF-S 60mm) supported on a custom-built horizontal slider above a transparent sample table made from Plexiglas. The camera slider could be programmed to automatically image samples in wells sequentially with defined timing. Lighting was provided by a 30 × 60 cm LED panel (Epistar, 4000 K, 960 lm) placed 20 cm below the sample table. The LED light was synchronized with the 12 h:12 h light:dark cycle of the culture chamber, and during the dark phase flashed for only 100 ms for imaging. Temperature was maintained at 25 °C, so the conditions in the imaging chamber were very similar to the phytochamber, but without shaking. Imaging in this setup provided a field of view of around 3 × 2 cm. Cells were imaged in transparent multiwell polystyrene cell culture plates (Corning® Costar®, Merck) that were placed onto the sample table and photographed from above.

Microfluidic setup. For observation and quantification of single filament motility and filament–filament interactions, a microfluidic device was designed with four separate 8 × 8 mm chambers per microscope slide, each with an inlet and an outlet (**Fig. S11**). With a 2× objective, one image

covered about 60% of a chamber. The chamber height of 85 µm was chosen to allow visual separation of filaments attached to the bottom or the top surfaces of the chamber by adjusting focus. To fabricate the microfluidic devices, a master was produced using standard photolithography techniques with Photoresist SU-8 3000 (purchased from KAYAKU Advanced Materials, .Inc). Individual microfluidic devices were made using polydimethylsiloxane (PDMS). The PDMS was produced by mixing SYLGARD 184 (Dow Inc.) Base and Curing Agent (10:1 ratio), pouring the mixture onto the master, and baking it at 80 °C for at least 3 h. Once hardened, the PDMS was separated from the master and bonded to a microscope slide after plasma treatment.

Filament behavior within the microfluidic chambers was imaged using a Nikon Eclipse Ti microscope equipped with an Andor Zyla sCMOS camera and 2× Nikon Plan Apo λ objective at 0.05 fps. The imaging light intensity, provided by a CoolLED pE-100, was set to 0.6% with an exposure time of 2.2 ms. An additional LED light source mounted on one side was used to adjust the light intensity to that in the growth phytochamber. Photosynthetically active radiation (PAR), measured using a light meter (WALZ ULM 500) with spherical sensor, varied between 50 and 78 µE, depending on measurement position (above or below the microfluidic chamber). The permeability of the PDMS upper surface of the microfluidic chambers allowed the exchange of gases.

Experiments

Experiments to characterize the response of aggregates to changes in light intensity

We used time-lapse imaging of *Trichodesmium* aggregates in the imaging chamber to quantify changes in aggregate shape and aggregate density as a response to changes in light intensity (**Fig. 1**).

Description. Stationary phase (~3 weeks since the last dilution) *T. erythraeum* cultures that showed aggregation in the bulk (naturally aggregating cultures) were used without adding new medium or filtering the cells. The culture was shaken gently until aggregates were completely dispersed into filaments, 3 mL of the dispersed culture was transferred to triplicate wells (34.8 mm diameter) of a 6-well cell culture plate (Corning® Costar®, Merck) and allowed to sediment for 1 h, and then the wells were imaged every 2 min for up to 36 h in the imaging chamber at 25 °C. In the first 10 hours, the aggregates were left to re-form in the wells, before the actual experiments began. Filaments were then exposed to one of two different light switching treatments, superimposed on the 12 h:12 h light:dark cycle in which the cultures had been grown (**Fig. 1**). These two treatments/experiments were done in different weeks. Technical replicates were done during each experiment, by distributing the experimental culture into triplicate wells as mentioned above. In one treatment, the light phase was interrupted by three successive 2 h-duration LIGHT OFF phases, leading to a ~1 h LIGHT ON, 2 h LIGHT OFF rhythm. Some variation was added to the LIGHT ON phases, so that they varied between 40 and 70 min, to distinguish responses to light from any possible responses associated with a circadian rhythm. In the other treatment, the dark phase was interrupted by three successive ~1 h-duration LIGHT ON phases, leading to a similar ~1 h LIGHT ON, 2 h LIGHT OFF rhythm as for treatment 1, but superimposed on the "night" instead of the "day". Note that the dark phase in the second

treatment (**Fig. 1D**) actually starts with a 2h-duration light phase, which is not a light switch, but just an extension of the daytime light phase, and did not induce an aggregate response. Only one of the technical triplicates from each treatment was used to produce Fig. 1, since the aggregates in the wells behaved very similarly, and each well produced enough aggregates to produce meaningful data.

To rule out the possibility that aggregates form and change shape or density passively, we performed an experiment comparing live and dead cells. For this, one well was filled with 3 mL of a dispersed filament sample and treated with 400,000 µJ UV in a Stratalinker. A second well was filled with a dispersed filament sample from the same culture without exposure to UV, and the plate was then imaged under constant light for 2 h. In contrast to the untreated culture, no aggregates formed in the UV-treated control, excluding purely physical explanations for aggregation.

Image analysis. To quantify changes in aggregate shape and aggregate density as a response to the light switches, the 3168 × 4752 pixel images were first converted to 8-bit greyscale images with ImageJ. Using a custom MATLAB script, pixel values were then divided by the trimmed (after removing the top 30% and bottom 30% of values) global mean to account for small differences in the captured light intensity due to the frequency of the LED. Aggregates were then segmented using a global threshold on the pixel intensity values, which delineated aggregates well (**Fig. S12)**. Segmented aggregates were hole-filled. For each detected aggregate, the weighted centroid position, pixel values, mean pixel intensity, area, eccentricity, aspect ratio, and pixel value sum were calculated. Aggregates with less than 2000 px^2 area and an eccentricity below 0.1 (almost perfectly round) were excluded. This removed most imaging artefacts such as air bubbles or dust, but also the smallest tuft aggregates (see **Fig. S12** for a demonstration of the retained particles). In order to measure how each aggregate's density (measured by the proxy "mean pixel intensity") changed over the course of the experiment, aggregates were tracked through space and time using a custom tracking algorithm, retaining only those tracked for at least 50 frames (100 min), and allowing aggregate position to change by a maximum of 500 px between frames.

Experiments to characterize the motility behavior of individual filaments and filament pairs

We used time-lapse video microscopy in the microfluidic setup to characterize the motility of individual filaments and filament pairs in non-aggregating and aggregating *Trichodesmium* cultures (**Fig. 2**).

Description. The rationale for this experiment was that the behavior that leads to aggregation should already be visible in the smallest possible aggregate – two encountering filaments. To characterize the motility of single filaments gliding on a surface and quantify their behavior upon encounter with a second filament, mid to late exponential cultures (13–14 d after last dilution) were imaged in the microfluidic setup for a minimum of 2 h, usually for around 4h, during the day. These cultures did not naturally aggregate. To investigate which aspects of motility change when a culture does aggregate, we split them into an experimental culture and a control culture and induced aggregation in the experimental culture by addition of 5 µM menadione as described in the section *Culture of Trichodesmium erythraeum* above. These cultures were then split

further and imaged both in the microfluidic setup and the imaging chamber in parallel. The latter served as confirmation of successful induction of aggregation in the experimental culture and non-aggregation in the control culture. Filament densities in the microfluidic setup were deliberately chosen to be too low to observe aggregate formation, so that interactions of pairs of filaments could be studied. Control and experimental cultures were imaged in the imaging chamber in two neighboring wells of a 6-well plate, to confirm non-aggregation and aggregation, respectively. Aggregation was checked by direct observation, without image analysis. If the control aggregated or the menadione-induced sample did not aggregate, the experiment was discarded. We report data from 12 biological replicates and experiments performed over 6 weeks.

To track single filaments, the four parallel chambers of the microfluidic device were filled with control or experimental culture samples. Chambers were first filled with mYBCII medium (without Fe and P to avoid introducing fresh nutrients) to reduce the number of bubbles entrapped during the filling process. The *Trichodesmium* filaments were then introduced into the chambers using a 1 mL pipette, displacing the mYBCII with their own spent medium. The four chambers were filled so as to alternate between aggregating induced cultures (chambers 1 and 3) and non-aggregating non-induced cultures (chambers 2 and 4). Mean density was 0.6 filaments mm^{-2} (range 0.1–1.4 filaments mm^{-2}), so that only a few pairs formed over the course of the experiment, allowing the tracking of filament–filament interactions without disturbance by other filaments. Filaments usually survived and glided for over 12 h in this setup. These experiments were performed with different cultures over multiple weeks and the motility data of all single filament tracks and filament–filament interactions were pooled.

The motility experiments in the microfluidic setup required a low filament density compared to the density of the used cultures, so we carried out experiments to confirm that the process of diluting mid-exponential, menadione-induced or control cultures did not change their general aggregation behavior. This "dilution-control" experiment was performed in the imaging setup. For these experiments, non-diluted samples were created by transferring 3 mL of a culture to one well of a 6-well plate. Diluted samples were created by transferring 100 µL of the same culture to a second well, which was then filled to 3 mL with the same culture filtered through a 5-µm filter syringe (which removed *T. erythraeum* filaments). Both wells were imaged to generate a time-lapse video (**Movie S10**) over 12 h and images from the dispersed filaments (before aggregation commenced) were segmented and thresholded to calculate filament densities. Aggregation was readily observed for both undiluted and 30×-diluted induced culture samples, and was not observed for undiluted or diluted control cultures (i.e., no stable aggregates formed, only short-lived, amorphous ones), confirming that dilution did not change aggregation behavior.

Image analysis. To extract tracks of single filaments and pairs of filaments, we analyzed the images taken in the microfluidic setup using a custom Python script described in detail in the Supplementary Text (**Fig. S13**). In the first processing step, all particles were tracked, classified, and extracted from the generated image sequences. In a second step, tracks of particles classified as filament pairs were further segmented to differentiate the two filaments in a pair. The output of the Phyton code (tracks of single filaments and pairs of filaments) was then used as an input to a custom Matlab code to compute gliding motility statistics (both codes are available here DOI: 10.3929/ethz-b-000596515).

Analysis of filament trajectories. To characterize the motility of individual filaments in a given condition, we analysed pooled tracks from 12 different experiments (**Fig. 2**, **Fig. S1**; see code 'analyze_single_filaments.m' in DOI: 10.3929/ethz-b-000596515). We restricted the analysis to tracks that were at least 50 frames (= 16 min) long. For example, to characterize the non-aggregating cultures, we obtained $n = 776$ individual tracks. To characterize the distribution of filament speeds, we combined time series representing speeds of individual filaments into a single time series (the resulting histogram of the filament speed is shown in **Fig. S1A**), which gave the reported mean speed and standard deviation. Once the mean filament speed had been obtained, it was used as a threshold to segment tracks into runs (segments with instantaneous speed greater than the mean) and reorientations (segments with instantaneous speed smaller than the mean) (**Fig. 2A, Fig. S1E, F**). In the non-aggregating control culture, segmenting the $n = 776$ tracks yielded $n = 2416$ runs and $n = 1518$ reorientations, which generated the distributions of run times, run lengths and reorientation angles (**Fig. 2B,C, E; Table S1**). Similarly, to estimate the reversal probability in a reorientation event, we combined all reorientation events from all tracks and treated them as independent events (Bernoulli trials). Each reorientation event was classified as a reversal if the reorientation angle was more than 90° and as a continuation of forward movement otherwise (**Fig. 2C**, **Fig. S1G**). The reversal probability was then estimated as the total number of reversals divided by the total number of reorientation events. To estimate the reversal frequency, we first computed the reversal frequency for each track, defined as the number of reversals divided by the track duration, and then averaged over tracks with weight proportional to the track length. The reported values for the mean and standard deviation of the reversal frequency are thus weighted by the track length. The motility of filaments in aggregating (menadione-induced) cultures were analysed analogously (**Table S1**).

To characterize the motility of filaments in pairs in a given condition, we started with the pool of tracks identified in the Python pipeline and then manually selected all tracks of filament pairs in which the filaments aligned with one another. For example, for the control, we obtained $n = 79$ pairs of such tracks representing pairs of aligned filaments (and thus $n = 158$ tracks in total, since there are two tracks per pair). We then segmented the tracks into runs and reorientations using the mean speed computed for the $n = 776$ tracks of individual filaments in the control (see code 'analyze_pairs.m' in DOI: 10.3929/ethz-b-000596515). That is, the speed threshold used to define runs and reorientations was the same for individual filaments and filaments in pairs. The analysis of the run times, run lengths and reorientations for filaments in pairs was then carried out in the same manner as for individual filaments. The motility of filaments in aggregating (menadione-induced) cultures were analysed analogously (**Table S1**).

Statistical analysis

To characterize filament motility, we analysed filament tracks from $n = 12$ independent motility experiments as described above. Each experiment contributed multiple tracks of filaments in aggregating (menadione-induced) and non-aggregating cultures. Combining these experiments, we obtained $n = 776$ tracks of individual filaments in non-aggregating cultures, $n = 643$ tracks of individual filaments in aggregating cultures and $n = 59$ pairs of tracks representing pairs of aligned filaments in aggregating cultures. The summary of all the quantities derived from the analysis of tracks of individual filaments or filaments in pairs is presented in **Table S1**.

Comparing individual filaments and filaments in pairs in aggregating cultures. In **Fig. 2E**, we rejected the null hypothesis that the two distributions of normalized run lengths for single filaments and filaments in pairs come from the same distribution, against the alternative hypothesis that the cdf (cumulative distribution function) of the run length distribution of filaments in pairs is larger than the cdf of the run length distribution of single filaments. This was based on the Kolmogorov–Smirnov two-sample one-sided test computed using the kstest2() function in MATLAB with the option 'Tail' set to 'Larger', which yielded the asymptotic p value $p = 2.97\times10^{-4}$ for the test statistic $k = 0.1125$ with sample sizes $n_{single} = 1964$ and $n_{pairs} = 377$. Additionally, we performed downsampling of the larger dataset by retaining, at random, only approximately 20% of single filament runs (so that $n_{single} = 393$, $n_{pairs} = 377$) and used the same test as before (Kolmogorov–Smirnov two sample, one-sided test computed using the kstest2() function in MATLAB with the option 'Tail' set to 'Larger'), which yielded $p < 0.05$ in ten such random trials.

Comparing the skewed Lack-of-overlap distribution with the uniform distribution. In **Fig. 2H**, we rejected the null hypothesis that the experimental distribution of the absolute Lack-of-overlap values comes from a uniform distribution on the interval [0, 1] against the alternative hypothesis that it does not come from a uniform distribution. This was based on the Kolmogorov–Smirnov one-sample two-sided test computed using the kstest() function in MATLAB, which yielded the asymptotic p value $p = 2.47\times10^{-10}$ for the test statistic $k = 0.4558$ with sample size $n = 53$ (see code 'analyze_pairs.m' in DOI: 10.3929/ethz-b-000596515). As samples, we took the $n = 53$ independent pairs of filaments that produced a non-zero Lack-of-overlap at some point during the observation time out of the $n = 59$ total observed pairs. That is, we excluded six pairs that were fully overlapped (Lack-of-overlap = 0) for the entire track duration since filaments in such pairs do not experience temporal changes in the overlap. Similarly, for the remaining $n = 53$ pairs, we restricted the Lack-of-overlap time series to non-zero values ($|\text{Lack-of-overlap}| > 0$) because only those instances where $|\text{Lack-of-overlap}| > 0$ correspond to changes in the overlap. Finally, each sample was then computed as the mean of the truncated time series of the absolute and non-zero values of the Lack-of-overlap. As an alternative approach, we selected an absolute non-zero Lack-of-overlap value ($|\text{Lack-of-overlap}| > 0$) at random from each pair rather than taking the mean over each entire track. In ten realizations of this test, each time, we obtained $p < 10^{-5}$.

Modelling of smart reversals and timescales of aggregation

The models are described in full detail in the Supplementary Text. To study the aggregation behavior of individual thigmotactic filaments (**Fig. 3**), we developed an agent-based model built upon the bead–spring model of active filaments (*62*) with the inclusion of overlap-induced reversals and random encounters with alignment in 3D (**Fig. S4-6**; **Supplementary Text Sections V, VIII and IX**). The model was implemented in the Julia Programming Language (v1.3.1). To estimate encounter-mediated aggregation timescales, we used mean field models described by encounter kernels (*63*) and the Smoluchowski coagulation equation (*64*). We simulated the coagulation equation in MATLAB (R2019a) with encounters modelled through a combination of encounter kernels for elongated aggregates settling in a quiescent fluid (*65, 66*), encounter kernels for identical rods mixed by turbulence (*43*) and for spherical aggregates mixed

by turbulence (*67*) (**Supplementary Text Section X**). Starting with initial conditions representing a suspension of individual filaments, we simulated the aggregation process until individual filaments were converted into aggregates, which yielded the encounter-mediated aggregation timescales (**Fig. S7**).

Supplementary Text

I. Image analysis of filament tracks

In the first image processing step, all particles were tracked, classified, and extracted from the experimental image sequences following the steps in **Fig. S13A** and described in detail in Section I.A below. In a second step, tracks of filament pairs were further segmented following the steps in **Fig. S13D** and described in detail in Section I.B below. The pixel size of captured images was 3.24 μm px^{-1}.

A. Particle tracking

The processing software was written in Python 3 (version 3.6.7) and requires the following packages: OpenCV 4.0.0 (*68*), Numpy 1.16.0, Scipy 1.2.0, Pandas 0.23.4. All processing was run on a DELL Inspiron 5559 Laptop with 4 Intel Core i7 2.5GHz processors.

1. Segmentation. The images were segmented into moving objects (foreground) and background by subtracting the median background image followed by thresholding. The median background image was calculated with 10% of all images to reduce computational time. The images were preprocessed by smoothing with a 7×7 Gaussian filter to reduce light variations. If filament densities inside the chamber were very high, the median background image contained filament residuals and was manually corrected with GIMP (GNU Image Manipulation Program, version 2.8.22).

The segmentation threshold was chosen based on trial-and-error and varied between 25 to 45 gray value intensity (8-bit) of the foreground image depending on lighting conditions. Due to high noise probability, we discarded particles close to the image border or microfluidics chamber wall (within a distance of 20 pixels).

2. Linking, merging, and splitting. The detected particles in different frames were connected to particle tracks by linking particles between subsequent frames and then linking track segments over multiple frames. Due to the low particle density, a simple nearest neighbor matching scheme was implemented to link particles or track segments (*69*). The scheme links particles j in frame t with particles k in frame $t + i$ in the order of ascending cost up to a maximal linking distance R_{max}. Since filaments move little between frames, the cost function was set to the Euclidean distance d_{jk} between the particles' centroids in frames t and $t + i$.

Particles were linked between subsequent frames up to a maximal distance of 5 pixels, which corresponds to about 16 μm. Track segment ends were connected to track segments starting between 1 to 4 frames later if the cost did not exceed $R_{max} = 40$ pixels (130 μm) and the length difference between particles j and k was smaller than 20 pixels (65 μm).

To study filament pair interactions, we implemented a merging and splitting algorithm to flag particle tracks consisting of two or more filaments (**Fig. S13A, B**). The flagged aggregate tracks and respective merged or split track numbers were stored for track classification (see 'Track classification' below). Four possible types of particle merging and splitting were distinguished: (1) two ending tracks merge into one starting track, (2) one ending track merges with a continuous track, (3) one ending track splits into two starting tracks, (4) one starting track splits

from the middle on another track (*70*). For events (2) and (4), the continuous track was split into a single filament and aggregate track.

The merging and splitting algorithm iterates through all frames in which a track segment ends (t_{end}) or starts (t_{start}) and evaluates first splitting and then merging events (**Fig. S13B**). If the minimal distance between the bounding boxes of particles *j* and *k* in frame *t* is smaller than 7 pixels (23 μm), the algorithm calculates the combined centroid (**Fig. S13C**):

$$\mathbf{C_{jk}} = \frac{\mathbf{C_j}A_j + \mathbf{C_k}A_k}{A_j + A_k}. \quad \text{(S1)}$$

Particles *j* and *k* are merged or split, if the difference between calculated aggregate centroid $\mathbf{C_{jk}}$ in frame *t* and actual particle centroid $\mathbf{C_l}$ in frame $t + i$ is smaller than 30 pixels (97 μm).

3. Track classification. The extracted tracks were subsequently validated and grouped into five classes: single filaments, interacting filament pairs, ghosting (non-interacting) filament pairs, multiple filament aggregates, and noise. The presented classification parameters were based on observations.

First, we removed some tracks as too intermittent. Tracks occasionally missed several frames due to, for example, failed filament segmentation or lack of match of filaments between successive frames. We discarded tracks with intermittency higher than 30%:

$$\frac{f_{i,end} - f_{i,start}}{n_i} < 1.3, \quad \text{(S2)}$$

where $f_{i,start}$ and $f_{i,end}$ are the starting and ending frame numbers and n_i is the total number of frames containing track *i*.

Single filament tracks were selected based on eccentricity and length variation. Eccentricity was calculated by fitting an ellipse using the OpenCV function fitEllipse() function (*68*). The eccentricity of a single filament was generally between 0.9 and 1. Specifically, tracks were classified as single filament tracks if they were labeled as aggregate tracks and fulfilled one of the following conditions:

$$\left\{\overline{e}_i > 0.98 \text{ and } c_{v,length,i} < 0.06\right\} \text{ or } \left\{\overline{e}_i > 0.93 \text{ and } c_{v,length,i} < 0.02\right\} \quad \text{(S3)}$$

where $\overline{e}_i$ is the track averaged eccentricity and $c_{v,length,i}$ is the coefficient of variation of particle length. Two different conditions were considered because shorter filaments have on average lower eccentricity.

Aggregate tracks were classified as filament pair tracks if both tracks that merged to form the filament pair or split from the pair were single filament tracks. If the mean ratio of eigenvalues [calculated using the Principal Component Analysis class in OpenCV (*68*)] was smaller than 0.02, the filaments were classified as interacting, otherwise as non-interacting.

Aggregate tracks not classified as filament pair tracks were labeled multiple filament aggregates. Similarly, tracks that were not labeled as single filament or aggregate tracks were classified as noise.

B. Segmentation of filament pairs

Tracks of filament pairs were further processed to separate the single filaments and to quantify their motion relative to each other according to the processing pipeline shown in **Fig. S13D**. The segmentation was based on a combination of distance and intensity thresholding, given that filaments were either overlapping vertically or horizontally, i.e., they were positioned next to or on top of each other (cf. **Fig. S13E**).

1. Distance transform. The distance transform *d* calculates the Euclidean distance of a pixel within an object to the closest boundary pixel and is therefore suited to flag adjoining filaments (**Fig. S13F**). For single filaments, *d* ranged consistently between 2 to 3 px, and for filament pairs situated side-by-side, between 4 to 5 px. The transform *d* was calculated using the OpenCV distanceTransform() function (*68*).

2. Normed intensity. Vertically stacked filament pairs are more effectively separated by intensity thresholding (**Fig. S13G**). The normed intensity was calculated as

$$I = \frac{I_{fg} - Q_{I_{fg},0.01}}{Q_{I_{fg},0.99} - Q_{I_{fg},0.01}}, \tag{S4}$$

where I_{fg} denotes the foreground intensity, which is the smoothed gray image (5×5 Gaussian blur) minus the background, and $Q_{I_{fg},i}$ is the i^{th} quantile within the object.

3. Weighting by overlap from the previous frame. Since filaments moved relatively slowly between subsequent frames, we could improve segmentation by further weighting the distance transform *d* and normed intensity *I* with a function of the overlap region from the previous frame (or the most recent, successfully matched frame). The weighting function $w_{prev,ov,d}$ of the distance transform *d* is heuristically defined as

$$w_{prev,ov,d} = (40 - r_{prev,ov})/40 \quad \text{if} \quad r_{prev,ov} < 40, \quad \text{and} \quad 0 \quad \text{otherwise}, \tag{S5}$$

where $r_{prev,ov}$ denotes the inverse distance transform from a background pixel to the boundary of the foreground object, here the overlap region of the previous frame. Similarly, the intensity weighting function $w_{prev,ov,I}$ is defined as

$$w_{prev,ov,I} = (15 - r_{prev,ov})^2/15 \quad \text{if} \quad r_{prev,ov} < 15, \quad \text{and} \quad 0 \quad \text{otherwise}. \tag{S6}$$

4. Distance and intensity threshold parameters. Depending on the relative positions of filaments, different threshold parameters for *d* and *I* separated the filament pair more effectively. Therefore,

the filament pair was segmented for different threshold parameters d^* and I^* out of a given parameter set, and the best cost-minimizing segmentation was subsequently chosen. The parameters were optimized on a finite option set because segmentation results were not sensitive to exact threshold values and for performance reasons.

Five parameter sets of d and I were heuristically obtained to cover different lighting conditions and were provided as input:

- $\{d > 4.0\}$,
- $\{d > 4.0\}$ or $\{d > 3.0$ and $I > 0.70\}$,
- $\{d > 4.0\}$ or $\{d > 3.0$ and $I > 0.85\}$,
- $\{d > 4.0\}$ or $\{d > 3.0$ and $I > 0.70\}$ or $\{d > 2.8$ and $I > 0.80\}$,
- $\{d > 4.0\}$ or $\{d > 2.6$ and $I > 0.55\}$ or $\{d > 2.0$ and $I > 0.65\}$.

The cost c was defined as the difference of input and segmented single filament length

$$c = [(l_1 - l_{1,in})^2 + (l_2 - l_{2,in})^2]^{0.5} \quad \text{(S7)}$$

where l_i is the length of filament i in the segmented image of the current frame and $l_{i,avg}$ is the input filament length (from merging and splitting algorithm in Section I.A).

If the cost exceeded 40 px, the segmentation was discarded, and a Nan-value was entered in the overlap time series.

5. Overlap region. The topological skeleton of the overlap region was retrieved by combining the thresholding results of d and I with thresholds (d^*,I^*). The entire overlap region (as in **Fig. S13H**) was determined by dilating the retrieved skeleton, connecting different regions, and clipping the region with the object foreground.

6. Allocation of the non-overlap region to filaments and Lack-of-overlap. The steps described above identified the region where the two filaments are overlapping. In a further step, the remaining regions, i.e., non-overlapping regions, were allocated to a specific single filament (**Fig. S13H**). From just looking at the gray image in **Fig. S13E**, it is impossible to determine if the smaller filament is completely overlapping with the longer filament or if it extends further. The allocation was therefore based on previous segmentation information or average filament lengths difference. Non-overlap regions were linked to regions in the previous frame with the linking algorithm described in Section I.A up to a maximal radius of 5 px. If they could not be linked, the ends were assigned to best match input filament lengths considering geometric relations. Based on the segmented filament pair sequence Lack-of-overlap was calculated to characterize the filament pair interaction.

II. Mechanisms of increase in reversal frequency for filaments in pairs vs. single filaments

In the Main Text, we reported that, in the menadione-induced cultures, the reversal frequency of filaments in pairs was nearly two-fold higher than for single filaments. Here we give more details on the mechanisms contributing to this reversal frequency increase.

There are three possible mechanisms of increase in the reversal frequency for filaments that perform runs and reorientations:

1. Increase in the probability p_{rev} of a reversal after a reorientation event. Each reorientation event, that separates subsequent runs, can either result in a reversal or the continuation of moving forward (**Fig. 2A**). We measured the reversal probability and found only a small difference between single filaments ($p_{rev} = 0.38 \pm 0.01$, mean ± sem, number or reorientation events $n = 1450$) and filaments in pairs ($p_{rev} = 0.40 \pm 0.03$, mean ± sem, $n = 266$; **Table S1**).
2. Increase in the overall activity as represented by the fraction of time f spent in the run mode. This mechanism can increase the overall number of reorientations by accommodating more runs in the same time interval. As reported in the Main Text, we found that filaments in pairs were more active ($f = 0.46 \pm 0.30$, weighted mean ± weighted sd, number of tracks $n = 118$, weight = track length) than individual filaments ($f = 0.35 \pm 0.32$, weighted mean ± weighted sd, $n = 643$; **Table S1**).
3. Change in the run length and run time. This mechanism also increases the overall number of reorientations by accommodating more runs in the same time interval. We measured changes in the normalized run length $l_{run}/l_{filament}$ (run length divided by filament length), physical (unnormalized) run length $l_{run,}$ and run time t_{run}. As reported in the Main Text, we found that filaments in pairs moved a smaller fraction of their length during a run, 35% less than single filaments (0.41 ± 0.85 vs. 0.63 ± 1.52, respectively; mean ± sd; $n_{runs,pairs} = 377$, $n_{runs,single} = 1964$; $p < 0.001$, two-sample one-sided Kolmogorov–Smirnov test, $k = 0.1125$) (**Fig. 2E**; **Table S1**; **Materials and Methods**). The same was true for unnormalized run lengths: filaments in pairs had shorter runs than individual filaments (239 μm ± 418 μm vs. 312 μm ± 650 μm, respectively; mean ± sd; $n_{runs,pairs} = 377$, $n_{runs,single} = 1964$; $p < 0.05$, two-sample one-sided Kolmogorov–Smirnov test, $k = 0.0731$). Finally, the run time t_{run} for filaments in pairs was shorter than for individual filaments (3.8 min ± 5.4 min vs. 5.2 min ± 8.2min, respectively; mean ± sd; $n_{runs,pairs} = 377$, $n_{runs,single} = 1964$; $p < 0.005$, two-sample one-sided Kolmogorov–Smirnov test, $k = 0.0947$).

As explained in Materials and Methods, we estimated the reversal frequency directly by first computing the reversal frequency for each track, defined as the number of reversals divided by the track duration, and then averaging over tracks with weight proportional to the track length. As reported in the Main Text, the reversal frequency was nearly two-fold higher in pairs than in single filaments (0.034 ± 0.040 min^{-1} vs. 0.019 ± 0.030 min^{-1}, respectively; weighted mean ± weighted sd; $n_{pairs} = 118$, $n_{single} = 643$; weight = track length). Taking the ratio of the means, we obtained a factor of 1.79. As an independent check, we note that the reversal frequency can be estimated by combining the three above mechanisms - the reversal frequency should be approximately equal to $p_{rev} f / t_{run}$. Taking the ratio $(p_{rev,pairs} f_{pairs} / t_{run,pairs}) / (p_{single} f_{single} / t_{run,single})$, we obtain the value of 1.89. We thus see that primarily the higher overall activity of filaments and shorter run times (or equivalently run lengths) contribute to the observed increase in reversal frequency.

III. Uniform vs. skewed 'Lack-of-overlap' distribution

The experimentally observed skewed distribution of the Lack-of-overlap values in filament pairs (**Fig. 2H** in the Main Text) starkly contrasts with the uniform distribution, suggesting that filaments perform smart reversals rather than reverse more often upon contact. Here, we provide more details on why the uniform distribution would be expected in the case of filaments that increase their reversal frequency when in contact with other filaments but do not further bias their motility to stay together.

First, we explicitly verified that a uniform distribution would be expected by directly simulating a model of motile filaments that glide on a surface, reverse randomly when not in contact with other filaments (with mean reversal frequency 0.2 min^{-1}) and double their random reversal frequency (mean 0.4 min^{-1}) when in contact with another filament (see Section IX.B below for more details about the simulation parameters). In multiple simulations (n = 32), each with 30 filaments, we identified all pairs of aligned filaments and measured their Lack-of-overlap, directly mimicking the experimental procedure. The corresponding histogram of the Lack-of-overlap values confirms the uniform distribution (orange line in **Fig. 2H** in the Main Text).

A simple analytical argument further rationalizes the expectation of a uniform distribution of Lack-of-overlap in the case of filaments that increase their reversal frequency when in contact with other filaments. Upon encounter and alignment, each filament in a pair performs a random walk with a contact-dependent step size. For example, in the simulations described in the previous paragraph, the mean step size is equal to the filament length when the filaments are not in contact and equal to half the filament length when in contact. We approximate an ensemble of such filament pairs and their relative positions as realizations of a one-dimensional diffusion equation with an effective diffusion coefficient that doubles upon contact ($D \rightarrow 2D$). Specifically, if the variable x denotes the relative position of the centroids of aligned filaments in a pair, then the distribution of filaments' relative positions $c(t,x)$ obeys the one-dimensional diffusion equation

$$\partial_t c = \nabla_x [D(x)\, \partial_x c], \quad \text{where} \quad D(x) = 2D \quad \text{if} \quad |x| < l \quad \text{and} \quad D(x) = D \quad \text{if} \quad |x| > l, \qquad \text{(S8)}$$

where l is the filament length. In the experiments and simulations, we identify and measure the Lack-of-overlap between aligned filaments in pairs whose initial relative positions are random due to random encounters on the substrate. Furthermore, different pairs are uncorrelated because they form at different locations and times. We interpret such measurements as independent samples from the steady-state solutions of Eq. (S8). The steady state solution is a constant $c(t,x) = C$, implying that filaments in pairs have no preferred relative position. Thus, all positions are equally likely to be observed, which rationalizes the observed uniform distribution of Lack-of-overlap in simulations. To illustrate this point better, consider, for example, a different experimental protocol in which all filament pairs were prepared to have their centroids aligned at the same initial time and then released – we would then seek solutions of Eq. (S8) that represent the initial value problem $c(0,x) = \delta(x)$, rather than the steady-state solution (*71*).

The uniform distribution would be expected even when the change in the reversal frequency depended not on binary contact but on the amount of overlap between the filaments. In this case, the effective diffusion $D(x)$ would be some function of x for $|x| < l$. But even in this case,

$c(t, x) = C$ solves the diffusion equation due to the balance of the diffusive flux $j(x) = D(x)\,\partial_x c = 0$. Thus, without an explicit mechanism that breaks the flux balance of incoming and outcoming filaments in pairs, no particular relative position is favored, and the uniform Lack-of-overlap distribution would be expected. By contrast, the additional reversals triggered by a temporal decrease in overlap in smart reversals break the flux balance and, on average, redirect filaments to stay together, which leads to a skewed distribution of Lack-of-overlap.

IV. Comparison of gliding motility statistics in pairs of filaments in menadione and exponentially growing control.

In this Section, we present an additional analysis of tracks of pairs of filaments in the control cultures and contrast their behavior with pairs of filaments in the menadione-treated cultures (**Figs. S2** and **S3**; **Table S1**). Specifically, this analysis shows that (i) filament pairs disintegrate 2.5 times faster in controls than in menadione-treated cultures, and (ii) filaments in the controls do indeed also exhibit some degree of smart reversals. This explains why control cultures, under the high filament density conditions exhibit some transient clustering (**Movie S10**) in the form of short-lived and amorphous aggregates. Overall, this analysis underscores how the formation of aggregates depends on filaments encountering each other (encounter rate) and on their ability to stay together (smart reversals). Working against this is the tendency of aggregates to fall apart due to the random movement of filaments.

First, by analyzing the interaction time of filaments in pairs we determined that pairs of filaments in the control spend less time together than pairs of filaments in menadione (16.8 min ± 24.4 min vs. 26.7 min ± 20.8 min; mean ± std; $n_C = 79$, $n_M = 59$). This observation is statistically significant ($p < 0.001$, two-sample one-sided Kolmogorov-Smirnov test). The corresponding cumulative distribution function (cdf) is shown in **Fig. S3A**. Comparing the means, we conclude that pairs of filaments in menadione spent 60% more time together than did pairs of filaments in the control. Thus, pairs of filaments in the control (where no formation of organized, lasting aggregates was observed; **Movie S10**) have briefer interactions than in menadione. This analysis prompted us to next determine the rate at which two filaments in a pair leave each other ('disintegration rate' λ_{dis}), in order to understand whether that rate of disintegration was different between menadione and control.

The pair interaction time alone does not allow one to determine how fast pairs of filaments disintegrate. In fact, in our experiments a pair of filaments can stop being a pair in one of three ways: (i) the pair disintegrates by splitting into two filaments, or (ii) the pair encounters a third filament, or (iii) the experimental recording ends. **Figs. S3B** and **S3C** summarize the three possibilities and shows the statistics of each possibility for both menadione and controls from our experimental data. Based on this, we compute the disintegration rate λ_{dis} from the mean interaction time tint (**Fig. S3A**) and the proportion of pairs f_{dis} that end by disintegrating (**Figs. S3B** and **S3C**), as

$$\lambda_{dis} = f_{dis} / t_{int}.$$

For example, in menadione 13 out of 59 pairs ended up disintegrating. Thus, $f_{dis} = 13/59$ and (with $t_{int} = 26.7$ min, see above) we find $\lambda_{dis} = 0.0082$ min^{-1}. Similarly, in controls 28 out of 79 pairs ended up disintegrating. Thus, $f_{dis} = 28/79$ and (with $t_{int} = 16.8$ min, see above) we find $\lambda_{dis} = 0.021$ min^{-1}. The ratio of disintegration rates

$$\lambda_{dis}^{control} / \lambda_{dis}^{menadione} = 2.56,$$

shows that filament pairs disintegrate 2.5-fold more rapidly in controls than in menadione. We highlight that, unlike the interaction time t_{int}, the disintegration rate is intrinsic to filament pairs (rather than being also a property of the filament density or the length of our recording, for

example), because it does not depend on the encounter rate with a third filament. We next investigated which factors explain this 2.5-fold difference in the disintegration rate.

To better understand the difference in the rate at which pairs of filaments disintegrate in menadione and control we focused on three traits: smart reversals, gliding velocity and filament length. We show in the following that all three traits are important in setting the timescale of pair disintegration.

We first investigated whether filaments in the control also exhibited a bias to stay together or rather performed random (not smart) reversals. **Fig. S3D** shows that filament pairs in both menadione and control perform smart reversals, as indicated by the skewness of the Lack-of-overlap histograms. The histogram for menadione is more skewed than for the control (mean 0.28 vs 0.30 and skewness 0.96 vs 0.75, respectively), implying stronger bias for menadione. This difference is however not statistically significant. We stress here that the skewed Lack-of-overlap histogram is a good indicator of the presence of smart reversals, since random reversals would lead to a flat distribution, but it does not by itself determine the disintegration rate. As shown by the corresponding trajectories of the Lack-of-overlap in each treatment (colored by how the tracks end, **Figs. S3E** and **S3F**), these similar histograms are dynamically realized by different trajectories, with many of the disintegration events in the control occurring over a short time (red curves) in line with the 2.5-fold difference in disintegration rates. To illustrate this point better, we highlight that even identical Lack-of-overlap histograms could have very different disintegration rates. For example, consider a pair of filaments that biases their motility to stay together but then eventually disintegrates. Then consider kinematically the same trajectory but executed twice as fast: while both trajectories would lead to the same Lack-of-overlap histogram, the latter would also result in twice as high a disintegration rate.

We next investigated the contribution of such kinematic effects, stemming from differences in filament gliding speed and length, and showed that they are partially, but not solely responsible for the higher disintegration rate between the control and menadione. Subsequently we will return to smart reversals.

Filament gliding speed and length are relevant for filament pair disintegration (and thus ultimately for aggregate formation) because they set the mean timescale $t_l = l/v$ that it takes a filament to glide its length. We thus first compared the distributions of filament lengths l and speeds v for menadione and control (**Fig. S2**). We found that filaments in pairs in menadione were slower (36.6 μm min^{-1} vs. 44.0 μm min^{-1}) and longer (743 μm vs. 651 μm) than in control. Quantitatively, we found that $t_l^{\text{menadione}}/\, t_l^{\text{control}} = 1.37$. This kinematic factor is too small, however, to explain the 2.5-fold difference in the disintegration rate. This can be seen from normalizing the disintegration rate λ_{dis} by t_l^{-1} and taking the ratio of such renormalized disintegration rates, as

$$(\lambda_{\text{dis}}^{\text{control}}/t_l^{\text{control}})/(\lambda_{\text{dis}}^{\text{menadione}}/t_l^{\text{menadione}}) = 2.56 / 1.37 = 1.87.$$

A ratio equal to one would suggest that the difference in disintegration rates between control and menadione stems entirely from how fast the tracks are executed. (It would also imply that the control has a faster reversal response to keep reversing fast enough to compensate for being faster and shorter.) Instead, the fact that the ratio is greater than one means that kinematics alone (gliding speed and length) are insufficient to explain the 2.5-fold higher disintegration rate of the control compared to menadione. In other words, filament pairs in menadione (compared to filament pairs in control) stay together longer than would be predicted based on their gliding

speed and length alone. This additional tendency to stay together is then a manifestation of stronger smart reversals. While filaments in both menadione-treated cultures and controls have a skewed Lack-of-overlap, filaments in menadione perform stronger thigmotaxis than filaments in the control, as we explore next. Later, in Section VI, we demonstrate using the agent-based model how the lower thigmotactic activity in the control - despite having a Lack-of-overlap skewed nearly as much as in menadione - results in the formation of transient clustering, which frequently disintegrate and thus do not form stable aggregates.

To further explore the role of smart reversals, we factor the disintegration rate into the following product

$$\lambda_{\text{dis}} = 2 f_{\text{rev}}\ p_{\text{esc}}\ \lambda_{\text{dis}},$$

where f_{rev} is the frequency at which a filament in a pair reverses and p_{esc} is the probability that the filament escapes (i.e., glides off another filament) because it failed to perform a reversal (the factor of two comes from having two filaments in a pair). In other words, each reversal event carries a risk of disintegration from a failure to perform a smart reversal, and this risk is quantified by p_{esc}. The stronger the smart reversal response, the lower p_{esc} will be. Since λ_{dis} and f_{rev} can be directly quantified from our data, and f_{rev} is nearly equal for menadione and control (0.034 ± 0.040 min^{-1} vs 0.033 ± 0.040 min^{-1}; mean ± std; $n_M = 119$, $n_C = 158$; **Table S1**), we can quantify the probabilities p_{esc} for menadione and control as

$$p_{\text{esc}}^{\text{menadione}} = 0.12 \pm 0.04 \qquad \text{and} \qquad p_{\text{esc}}^{\text{control}} = 0.31 \pm 0.08.$$

Thus, filaments in the control have a substantially higher probability of failing to perform smart reversals. Consequently, filaments in menadione glide off after on average $1/p_{\text{esc}}^{\text{menadione}} \sim 8$ reversals, and filaments in control after on average $1/p_{\text{esc}}^{\text{control}} \sim 3$ reversals. (Or, since there are two filaments in a pair and either of them may glide off, it takes respectively about 4 and 1.5 reversals before one of the two filaments in a pair glides off and the pair disintegrates). In Section VI, we describe how to use the probability p_{esc} to derive the response time τ of smart reversals implemented in the agent-based model.

V. 2D bead-spring model for filaments on a surface

In this section, we present the details of our model of aggregation by *Trichodesmium* filaments on a surface through gliding and smart reversals (**Fig. S4**). Building on the model introduced by Isele-Holder, Elget, and Gompper (*62*) and equipping it with smart reversals, we represent *Trichodesmium* filaments as self-propelled semi-flexible rods composed of $N + 1$ beads (**Fig. S4A**) that obey the following over-damped dynamics

$$\gamma \boldsymbol{v}_i^\alpha = \gamma \frac{\partial \boldsymbol{x}_i^\alpha}{\partial t} = -\frac{\delta U}{\delta \boldsymbol{x}_i^\alpha} + \boldsymbol{F}_i^\alpha, \tag{S9}$$

where $\boldsymbol{x}_i^\alpha$ and $\boldsymbol{v}_i^\alpha$ represent the position and velocity of the i-th bead of the α-th filament, U is the configurational energy, $\boldsymbol{F}_i^\alpha$ represents the gliding forces of the i-th bead of the α-th filament, and γ is the friction coefficient. Simulations in 2D (described below) were performed on a square domain with side length L_{box} with periodic boundary conditions and with initial conditions corresponding to filaments' centers of mass placed on a square grid with random orientations.

A. Standard passive and active interactions

The configurational energy functional is a sum of the self-interaction energies of each filament and filament–filament interactions

$$U = \sum_\alpha \; U_{\text{sf}}^\alpha \; + \; \sum_{\beta \neq \alpha} \; U_{\text{ff}}^{\alpha\beta}. \tag{S10}$$

1. Self-interaction energy. The self-interaction energy of a single filament represents the contributions due to elastic and bending energies

$$U_{\text{sf}}^\alpha(\{\boldsymbol{x}_i^\alpha\}) = \text{elastic} + \text{bending} = \sum_{i=1}^{N} \; u_{\text{e}}(\|\boldsymbol{r}_i^\alpha\|) + \sum_{i=1}^{N-1} \; u_{\text{b}}(\boldsymbol{r}_i^\alpha, \boldsymbol{r}_{i+1}^\alpha), \tag{S11}$$

where $\boldsymbol{r}_i^\alpha = \boldsymbol{x}_{i+1}^\alpha - \boldsymbol{x}_i^\alpha$ is the bead-to-bead vector. The energies of each elastic and bending bond are (*62*)

$$u_{\text{e}}(\|\boldsymbol{r}_i^\alpha\|) = \frac{k}{2}(\|\boldsymbol{r}_i^\alpha\| - r_0)^2, \tag{S12}$$

$$u_{\text{b}}(\boldsymbol{r}_i^\alpha, \boldsymbol{r}_{i+1}^\alpha) = \frac{\kappa}{4}(\boldsymbol{r}_i^\alpha - \boldsymbol{r}_{i+1}^\alpha)^2 \,, \tag{S13}$$

where k is the elastic spring constant, r_0 is the equilibrium bond length, and κ is the bending rigidity. We set the values of k and κ large enough to impose the limit of inextensible and nearly rigid filaments (Section IX).

2. Filament–filament interaction energy. The filament–filament potential energy represents short-range steric repulsion and attraction (**Fig. S4B**)

$$U_{\text{ff}}^{\alpha\beta}(\{\boldsymbol{x}_i^\alpha\}, \{\boldsymbol{x}_j^\beta\}) = \sum_{i=1}^{N+1} \; \sum_{j=1}^{N+1} \; u_{\text{s}}(\|\boldsymbol{x}_i^\alpha - \boldsymbol{x}_j^\beta\|), \tag{S14}$$

via the truncated Lennard-Jones potential

$$u_s(r) = 4\epsilon[(\sigma/r)^{12} - (\sigma/r)^6], \quad r < 1.25\sigma \quad \text{and} \quad 0 \quad \text{for } r > 1.25, \tag{S15}$$

where ϵ is the volume-exclusion energy and σ is the effective filament diameter (bead size). The range $\sigma < r < 1.25\ \sigma$ represents attractive interaction between filaments mediated by the exudation of exopolymers and appendages and was guided by previously reported scanning electron microscopy images (*12*).

3. Active gliding. Each filament exerts a propulsion force on the substrate and nearby filaments (**Fig. S4A**). The propulsion force is distributed along the filament, on each bead, and is oriented along the filament's long axis. Specifically, let the unit tangent vector along each bead on a filament be defined as

$$\boldsymbol{t}_i^\alpha = (\boldsymbol{x}_{i+1}^\alpha - \boldsymbol{x}_{i-1}^\alpha)/\|\boldsymbol{x}_{i+1}^\alpha - \boldsymbol{x}_{i-1}^\alpha\|, \quad 1 < i < N+1, \tag{S16a}$$

$$\boldsymbol{t}_1^\alpha = \boldsymbol{t}_2^\alpha, \quad \boldsymbol{t}_{N+1}^\alpha = \boldsymbol{t}_N^\alpha. \tag{S16b}$$

The propulsion force on bead i on filament α is then

$$\boldsymbol{F}_i^\alpha = -f^\alpha \boldsymbol{t}_i^\alpha + \sum_{\beta \neq \alpha} \sum_{j=1}^{N+1} (f^\beta \boldsymbol{t}_j^\beta - f^\alpha \boldsymbol{t}_i^\alpha)\delta(\boldsymbol{t}_i^\alpha, \boldsymbol{t}_j^\beta, \boldsymbol{x}_i^\alpha, \boldsymbol{x}_j^\beta), \tag{S17}$$

where $f^\alpha = \pm f$ is the strength of the force source on each bead - the magnitude f is fixed, but it can have either sign, which can change due to reversals, as described in the next section. The first term in Eq. (S17) represents the propulsion force exerted by the substrate on the bead - the reaction force due to the action of the bead on the substrate. The second term is a sum of action–reaction forces on bead i of filament α due to all beads on all other filaments that are sufficiently close and sufficiently well-aligned. These proximity and alignment conditions are

$$\delta(\boldsymbol{t}_i^\alpha, \boldsymbol{t}_j^\beta, \boldsymbol{x}_i^\alpha, \boldsymbol{x}_j^\beta) = 1 \quad \text{if } \|\boldsymbol{x}_i^\alpha - \boldsymbol{x}_j^\beta\| < 1.25\sigma \text{ and } |\boldsymbol{t}_i^\alpha \cdot \boldsymbol{t}_j^\beta| > \cos(\pi/18), \quad \text{and} \quad 0 \quad \text{otherwise.} \tag{S18}$$

The proximity condition is the same as the truncation distance in the Lennard-Jones potential (S15), and the alignment condition corresponds to the tangent vectors pointing at most 10° away from each other. These conditions are motivated by our micropipette experiments, which show that filaments only start pulling onto each other when well-aligned (**Movie S7**).

B. Overlap sensing and reversals

The propulsion force on each filament can reverse its direction from parallel to anti-parallel due to sensing the Lack-of-overlap with other filaments or due to an overlap-independent, slow reversal frequency (**Fig. S4B–E**).

1. Definition of overlap. We assume each filament can sense and monitor its overlap with all nearby filaments. We define the time-dependent overlap $\Theta^{\alpha}(t)$ of a filament α using an effective Lennard-Jones potential as

$$\Theta^{\alpha}(t) = -\frac{1}{N+1}\sum_{i=1}^{N+1}\ \sum_{\beta\neq\alpha}\ \sum_{j=1}^{N+1}\ \hat{u}_{\mathrm{s}}(\|\boldsymbol{x}_i^{\alpha} - \boldsymbol{x}_j^{\beta}\|), \tag{S19}$$

where

$$\hat{u}_{\mathrm{s}}(r) = 4[(\sigma/r)^{12} - (\sigma/r)^{6}],\ r < 2^{7/6}\sigma,\ \text{ and }\ 0 \text{ otherwise.} \tag{S20}$$

Above, σ is again the bead diameter [as in Eq. (S15)], but the potential has a larger truncation distance $2^{7/6}\sigma \approx 2.24\,\sigma$ (**Fig. S4B**). This larger truncation distance is introduced for computational reasons to avoid the introduction of more than one overlap sensor per bead. The negative sign in Eq. (S19) implies that $\Theta^{\alpha}(t)$ is positive for overlapping filaments; the larger the value, the larger the overlap. $\Theta^{\alpha}(t)$ represents the average coordination number of beads on the filament α. That is, $\Theta^{\alpha}(t)$ is the number of beads on other filaments in contact with a given bead on filament α, averaged over all beads on filament α. $\Theta^{\alpha}(t)$ can take non-integer values because our definition of bead–bead overlap is given by the Lennard-Jones potential rather than a binary variable.

2. Sensing Lack-of-overlap. In the model, filaments cam detect temporal gradients in $\Theta^{\alpha}(t)$ as follows. Each filament samples $\Theta^{\alpha}(t)$ at equally spaced time intervals, every τ_{Θ}, resulting in a discretized time series of the past overlap values $\{\Theta^{\alpha}(t_k),\ k = 0,\ 1,\ 2,\ldots\}$, where $t_k = t_{\mathrm{r}} - k\tau_{\Theta}$, and t_{r} denotes the time of the most recent measurement. From this discrete time series, the filament keeps only a short register of three such past values

$$\text{time-series register} = [\Theta^{\alpha}(t_{\mathrm{r}} - 2\tau_{\Theta}), \Theta^{\alpha}(t_{\mathrm{r}} - \tau_{\Theta}), \Theta^{\alpha}(t_{\mathrm{r}})]. \tag{S21}$$

When a new overlap sensing event occurs (every τ_{Θ}), the register is updated by a time-shift so that the three most recent values are always stored. The temporal gradient $TG^{\alpha}(t)$ in $\Theta^{\alpha}(t)$ at time t is then estimated as

$$TG^{\alpha}(t) = [\Theta^{\alpha}(t_{\mathrm{r}}) - \Theta^{\alpha}(t_{\mathrm{r}} - 2\tau_{\Theta})]/(2\tau_{\Theta}). \tag{S22}$$

3. Smart reversals. When the temporal gradient of overlap $TG^{\alpha}(t)$ is sufficiently negative, the propulsion force f^{α} changes sign after an exponentially distributed time with mean τ (the response time), resulting in a reversal of the direction of propulsion of the filament. For sufficiently negative, we take values smaller than $-2f/[(N+1)\sigma\gamma]$, which approximately represents the rate of decrease of overlap for a pair of aligned, overlapped filaments moving apart in opposite directions. Thus, the time-discretized version of the reversal criterion is

$$\text{if } TG^{\alpha}(t) < -2f/[(N+1)\sigma\gamma] \text{ then change the sign of } f^{\alpha} \text{ with probability } \Delta t/\tau, \tag{S23}$$

where Δt is the time-step of the simulation. Furthermore, when such a smart reversal occurs, the time-series register in Eq. (S21) is reset by setting

$$[\Theta^{\alpha}(t_{\mathrm{r}} - 2\tau_{\Theta}), \Theta^{\alpha}(t_{\mathrm{r}} - \tau_{\Theta}), \Theta^{\alpha}(t_{\mathrm{r}})] \rightarrow [\Theta^{\alpha}(t_{\mathrm{r}}), \Theta^{\alpha}(t_{\mathrm{r}}), \Theta^{\alpha}(t_{\mathrm{r}})]. \tag{S24}$$

Thus, after a smart reversal occurs, a filament starts to build temporal information on the state of its overlap again, starting from a uniform state.

In addition, all filaments perform reversals independently of overlap, with a slow, exponentially distributed reversal rate with mean $\tau_{\mathrm{random}}^{-1}$.

VI. Measurement of the response timescale from pair disintegration rates.

Here, we describe how the probability p_{esc} that a filament in a pair escapes (i.e., glides off another filament) because it failed to perform a reversal can be approximately related to the response time τ of smart reversals implemented in our model. In the model, the probability that a filament, once it detects that it starts to lose overlap, fails to reverse after time *t* is given by the exponential distribution $p_{esc}^{model}(t) = \exp(-t/\tau)$. To connect $p_{esc}^{model}(t)$ with the experimentally determined value of p_{esc} (Section IV), we assume that the relevant timescale over which disintegration may occur is given by the filament run time t_{run}. That is, we assume that if a filament does not reverse during a time equal to the mean run time (similar for both conditions, 3.8 ± 4.1 min vs 3.8 ± 5.4 min; mean ± sd; n_C = 312, n_M = 377; **Table S1**), then it disintegrates. Setting $\exp(-t_{run}/\tau) = p_{esc}$ and solving for τ yields

$$\tau = -t_{run}/\log(p_{esc}).$$

Using the experimentally determined values p_{esc} and t_{run} in the latter equation we find (**Table S1**)

$$\tau^{menadione} = 1.82 \pm 0.13 \text{ min} \quad \text{and} \quad \tau^{control} = 3.32 \pm 0.28 \text{ min}.$$

Thus, the response time of smart reversals for the control is about 80% longer than for menadione, meaning that filaments in the control perform smart reversals after a longer time than filaments in menadione, which increases their risk of disintegration. (The errors on the mean are computed with standard error propagation formulae). For better comparison with the model, we next normalize the experimental τ by the time to glide the filament length as follows (**Table S1**)

$$\tau^{menadione}/t_l^{menadione} = 0.09 \pm 0.01 \quad \text{and} \quad \tau^{control}/t_l^{control} = 0.22 \pm 0.02.$$

Thus, filaments in menadione have more than twofold shorter relative response times than filaments in the control. That is, filaments in pairs typically travel for less than 10% (in menadione) and for more than 20% (in controls) of the time needed to glide one body length, respectively, before they perform a smart reversal. It is this normalized quantity that we next compare with the model. We recall that in the model filaments sample overlap with rate τ_Θ and it takes them about $2\tau_\Theta$ = 10 s to detect that they are losing overlap. After detection, filaments in the model respond with a smart reversal after a time τ_{model} = 0.75 s, 12 s and 75 s for strong, intermediate, and weak thigmotaxis. Furthermore, when moving in isolation, filaments in the model move at a speed of 32 μm min^{-1}, but when in contact and fully overlapped, their speed is nearly two-fold higher since they additionally pull on each other (in addition to pulling on the substrate). Thus, for filaments in a pair moving in opposite directions and risking separation, the three model conditions of strong, intermediate and weak thigmotaxis correspond to traveling about 4%, 15% and 55% of a filament length before performing a smart reversal. Compared with experiments, we thus conclude that filaments in menadione approximately represent medium-to-strong thigmotaxis in the model, whereas filaments in the control represent weak-to-medium thigmotaxis in the model.

To better illustrate and sum up how the model can represent the two experimental conditions (menadione and control), their Lack-of-overlap and overall aggregation, we carried out

additional simulations to mimic the two conditions as follows (**Fig. S5C-F**). In the model, we represented menadione conditions by the triple (l,v,τ) = (160 μm, 32 μm min^{-1}, 4.2 s), which represents a condition such that a pair of filaments travels about 10% of a filament length before performing a smart reversal, as indicated by experiments. Control conditions were then represented in the model by making filaments 20% faster in their gliding, 10% shorter and with an 80% longer response time than menadione filaments, again as indicated by the experiments. Mimicking our millifluidic experiments, we then simulated 49 filaments moving on a surface for each condition. We found that the control condition reached a lower overlap level than in menadione (**Fig. S5C-E**) because filaments in the control formed aggregates that disintegrated more frequently and despite having the Lack-of-overlap nearly as skewed as in menadione (**Fig. S5F**).

VII. Thigmotactic response of slow vs. fast and short vs. long filaments.

Focusing again on the experiments, to further strengthen the understanding of the role of filament length and speed, we quantified (for each of menadione and control) p_{esc} and τ/t_l separately for short (< 600 μm) and long filaments (> 600 μm), as well as for slow (< 40.3 μm min^{-1}) and fast filaments (> 40.3 μm min^{-1}). The results (**Table S2**) show that (i) slower filaments have lower escape probabilities and response times than faster ones and (ii) longer filaments have lower escape probabilities and response times than shorter ones. These differences occur within each of the two treatments (menadione and control) and are even stronger across treatments: short filaments in the control have more than six-fold higher the escape probability than long filaments in menadione; and fast filaments in the control have more than five-fold higher the escape probability than slow filaments in menadione. As a final cross-check, we plot the cumulative distribution functions of the mean Lack-of-overlap (per track) for these extreme cases (**Figs. S3G** and **S3H**), and note that the differences in the Lack-of-overlap are more pronounced, as expected. For the long/short division, the difference is statistically significant, whereas for the fast/slow division the p value is just above 0.05. The point of this last check is to note that the Lack-of-overlap data responds as expected when the escape probability changes. In particular, as p_{esc} decreases, the Lack-of-overlap becomes smaller.

VIII. 3D bead-spring model for aggregate formation

To study the role of smart reversals in the formation of organized *Trichodesmium* aggregates in a liquid suspension (i.e., away from solid surfaces), such as in the ocean, we extended our bead–spring model to 3D. Apart from the change in dimensionality, the model for *Trichodesmium* aggregation in 3D differs in three fundamental ways from the 2D model on a substrate: (1) the traction force on the substrate is absent, (2) encounters between filaments happen through effective diffusion of a single seed filament, and (3) external torques are present, which align filaments upon encounter. Apart from these three modifications, discussed in detail below, all other parameters and interactions carry from the 2D model to 3D unchanged. Therefore, in 3D, the 2D equations of motion (S9) are replaced by

$$\gamma \boldsymbol{v}_i^\alpha = \gamma \frac{\partial \boldsymbol{x}_i^\alpha}{\partial t} = -\frac{\delta U}{\delta \boldsymbol{x}_i^\alpha} + \boldsymbol{F}_i^\alpha + \boldsymbol{D}_i^\alpha + \boldsymbol{T}_i^\alpha, \tag{S25}$$

where U is the same configurational energy as in Eq. (S10) and $\boldsymbol{F}_i^\alpha$, $\boldsymbol{D}_i^\alpha$ and $\boldsymbol{T}_i^\alpha$ represent gliding, diffusion, and aligning torques, as discussed next.

1. Active gliding. Since there is no substrate to glide on in the open ocean, the active gliding forces in 3D do not include the interaction with the substrate term in Eq. (S17) and thus reduce to

$$\boldsymbol{F}_i^\alpha = \sum_{\beta \neq \alpha} \sum_{j=1}^{N+1} \left(f^\beta \boldsymbol{t}_j^\beta - f^\alpha \boldsymbol{t}_i^\alpha \right) \delta\left(\boldsymbol{t}_i^\alpha, \boldsymbol{t}_j^\beta, \boldsymbol{x}_i^\alpha, \boldsymbol{x}_j^\beta \right). \tag{S26}$$

Only the terms that represent action–reaction pulling between individual filaments are retained. All other parameters remain as in the 2D case.

2. Encounters by effective diffusion. Building on the ideas of the classical kinetic aggregation of colloids (*72*), we model encounter-driven aggregate formation as an effective diffusion process, in which a single 'seed' filament performs a random walk and collects randomly distributed and randomly oriented filaments occupying a three-dimensional volume (**Fig. S6A**). All filaments that enter into contact with the seed filament start to diffuse with the seed filament, collecting other filaments, while the rest remain stationary. Equivalently, to keep the growing aggregate in the center of the simulation domain, we model the case as though the aggregate is fixed at the center of the domain, and the filaments not in contact with the aggregate perform the same Brownian dynamics until they encounter the aggregate. Specifically, the Brownian dynamics term $\boldsymbol{D}_i^\alpha$ in Eq. (S25) is implemented as follows

$$\boldsymbol{D}_i^\alpha = I^{\alpha \neq \Omega} \sqrt{2D} \boldsymbol{\xi}, \tag{S27}$$

where D is the effective diffusion coefficient and $\boldsymbol{\xi}$ is a 3D Wiener process - for time-discretized dynamics with time step Δt, each entry of $\boldsymbol{\xi}$ is sampled from a normal distribution with zero mean and variance Δt, independently at each time step. The indicator function $I^{\alpha \neq \Omega}$ is 1 if the filament α is not a member of the growing aggregate, members of which are listed in the list $\boldsymbol{\Omega}$, and 0 otherwise. Note that the same $\boldsymbol{\xi}$ is applied for all non-members of the aggregate at each

time step. This choice guarantees that single filaments arrive at the growing aggregate one at a time (*72*).

In simulations, this encounter model is realized in a cubic domain $[-L_{\mathrm{box}}/2,\ L_{\mathrm{box}}/2]^3$ with side length L_{box} and periodic boundary conditions. It is initialized by distributing ten filaments at random positions and with random orientations; the configuration is then translated to place the initial seed filament at the origin. Merging with the growing aggregate is defined as follows: if the distance between filament α and any of the members listed in $\boldsymbol{\Omega}$ is smaller than 1.25σ, the cut-off criterion used in the definition of stickiness in Eq. (S15), then the filament α becomes a member of the aggregate and the list $\boldsymbol{\Omega}$ is enlarged by α.

3. External torques. Upon encounter, filaments form rotational bonds and then experience torques due to external factors, such as differential sinking or turbulence. Our micropipette experiment clearly shows that bonds between filaments are rotational (**Movie S7**). We describe the action of external torques by introducing effective aligning torques $\boldsymbol{T}_i^{\alpha}$ that are implemented as follows. Consider first a pair of filaments α and β in contact with each other (**Fig. S6B**); contact is defined by the same filament–filament distance cut-off 1.25σ as implied by stickiness. We take the rotational bond to form between beads i', j', belonging to filaments α, β, that are closest to each other. The torques are realized by the following forces acting on beads adjacent to the beads i', j' (**Fig. S6B**)

$$\boldsymbol{T}_i^{\alpha} = \Gamma \mathrm{sgn}(\boldsymbol{t}_{i'}^{\alpha} \cdot \boldsymbol{t}_{j'}^{\beta})(\delta_{i,i'-1}\boldsymbol{t}_{j'}^{\beta} - \delta_{i,i'+1}\boldsymbol{t}_{j'}^{\beta}), \tag{S28a}$$

$$\boldsymbol{T}_j^{\beta} = \Gamma \mathrm{sgn}(\boldsymbol{t}_{i'}^{\alpha} \cdot \boldsymbol{t}_{j'}^{\beta})(\delta_{j,j'-1}\boldsymbol{t}_{i'}^{\alpha} - \delta_{j,j'+1}\boldsymbol{t}_{i'}^{\alpha}), \tag{S28b}$$

where Γ specifies the strength of the external torques and sgn() is the sign function. If i', j' happen to be the endpoints of the filaments ($i', j' = 1,\ N+1$), the above rotary bonds and torques are formed about $i', j' = 2$ or $i', j' = N$ beads.

If a filament α is connected to more than one filament, then it forms a rotational bond with each of them and is acted upon by torques of the form in Eq. (S28) coming from each pair.

IX. Bead-spring model parameters

Here, we state and motivate our choices of the parameter values for the bead–spring models and the corresponding simulation parameters. The values are guided by the principle that the characteristic timescales in the models should respect the same ordering as the timescales characterizing *Trichodesmium* aggregation in the ocean (**Fig. S7C**), which are identified experimentally or from calculations.

A. Model parameters

The parameter values characterizing filaments are summarized in **Table S3**.

1. Nondimensionalization. The friction coefficient γ in the over-damped dynamics in Eq. (S9) and Eq. (S25) only affects the overall timescale of the dynamics. We thus divide these equations by γ, which results in the model parameters acquiring the units of length and time. For example, $[k/\gamma] = T^{-1}$, $[\kappa/\gamma] = T^{-1}$, $[\epsilon/\gamma] = L^2T^{-1}$, and $[f/\gamma] = LT^{-1}$. As the characteristic timescale T and lengthscale L, we set T = 15 s, the time an individual filament gliding at speed 32 μm min^{-1} (**Table S3**) travels distance L, where L = 8 μm is approximately the filament width, *i.e.*, the size of a single cell. In simulations, we work with dimensionless parameters expressed in units of T and L, denoted by the prime symbol below.

2. Filament size. In the bead–spring model, the effective filament length and width are $(N+1)r_0$ and σ (Section V). We always discretize filaments into $N + 1 = 20$ beads. Since we take each bead to represent a single *Trichodesmium* cell, we set the cell–cell distance at $r_0 = \sigma$. In simulations, we take $r_0' = \sigma' = r_0/L = \sigma/L = 1$. In physical units, the model thus represents filaments with dimensions 8 μm × 160 μm.

3. Potentials and propulsive forces. In simulations, the magnitude f' of the propulsive forces on each bead is set at $f' = f/\gamma/(LT^{-1})$. This choice, in physical units, represents a gliding speed of 32 μmmin^{-1} for individual filaments gliding on a substrate, a value in agreement with the typical observed gliding speeds on a glass surface in our microfluidic chambers (**Table S1**).

We set the elastic spring constant k and the bending rigidity κ large enough to work within the limit of inextensible and nearly rigid filaments (large persistence length). Since deformations in the system are mainly produced by the propulsion force, to guarantee that extensional and bending deformations are small, we must choose $k \gg f/\sigma$ and $\kappa \gg f/\sigma$. In simulations, we thus set $k' = k/\gamma/T^{-1}$=500 and $\kappa' = \kappa/\gamma/T^{-1} = 2000$.

For the Lennard-Jones potentials in Eq. (S15) and Eq. (S20), the first parameter $\sigma' = \sigma/L = 1$ is set by the filament width, as described above. The potential strength ϵ is chosen small enough such that the attractive interactions between beads (stickiness) do not immobilize the filaments by overcoming the propulsion forces, yet large enough not to lead to aggregate disintegration under small perturbations arising from the propulsive forces, external torques, or small deformations that may occur in a bundle of interacting filaments. This self-consistency criterion is motivated by experimental observations that aggregates, once formed, remain stable yet dynamic, with filaments constantly gliding and reversing. We thus expect that $\epsilon \approx f\sigma$, which corresponds to stickiness forces having a similar magnitude to propulsion forces. In simulations we set $\epsilon' = \epsilon/\gamma/(L^2T^{-1}) = 1$.

4. Overlap detection and reversals. Each filament samples its total overlap $\Theta^{\alpha}(t)$ and compares the most recent value $\Theta^{\alpha}(t_{\mathrm{r}})$ with a value from the recent past $\Theta^{\alpha}(t_{\mathrm{r}} - 2\tau_{\Theta})$ [Eq. (S19) and Eq. (S22)]. Sampling of $\Theta^{\alpha}(t)$ occurs every τ_{Θ}, and we estimate this sampling time interval assuming that it is limited by how rapidly a filament can integrate the overlap signal from individual cells along its long axis. We assume that cell–cell communication along the filament length is limited by diffusion and combine two simple scaling arguments with experimental data to estimate τ_{Θ} (**Fig. S9**).

We estimate τ_{Θ} as the time it takes a signal to travel between the ends of a filament. We use diffusive and quasi-diffusive scaling arguments for a filament of length l and a signaling molecule with diffusion constant D. In the diffusive model, we assume that the filament is a one-dimensional tube with no compartments representing cells (**Fig. S9B**). In this case, $\tau_{\Theta} \approx l^2/2D$, scales quadratically with the filament length. In the quasi-diffusive autoinducer model, we take the filament to be composed of l/σ cells, each of length σ. It takes approximately $\sigma^2/(6D)$ for the signaling molecule to spread across each three-dimensional cell. Once a single cell equilibrates the signal within its volume, the neighboring cell detects the signal through hypothetical receptors in the dividing walls and starts producing the signal within its own volume. In this autoinducer model, $\tau_{\Theta} \approx l\sigma/6D$, scales linearly with the filament length. A small signaling molecule, such as the ubiquitous cyclic di-GMP messenger, will have $D \approx 300$ $\mu m^2\,s^{-1}$ in water (*73*) and $D \approx 100 \mu m^2\,s^{-1}$ in the crowded cell interior (*74*). To connect these considerations with our measurements of pairs of interacting filaments, we now approximate the sensing timescale τ_{Θ} as the time T_{LoI} needed for a filament in a pair to glide at its mean speed, a distance corresponding to the value of Lack-of-overlap at the instance of reversal, which we estimated from the tracks of pairs of filaments (**Fig. S9A**). Taking $\tau_{\Theta} \approx T_{\mathrm{LoI}}$, we see from **Fig. S9C** that τ_{Θ} falls between the two scaling regimes. In our simulations, the filament length is $l = 160$ μm, and the cell size is $\sigma = 8$ μm. For $D = 100$ $\mu m^2\,s^{-1}$, the diffusive scaling yields $\tau_{\Theta} \approx 130$ s, and the quasi-diffusive (autoinducer) scaling gives $\tau_{\Theta} \approx 2.1$ s. In simulations, we use the intermediate value $\tau_{\Theta} = 5$ s. We thus set $\tau'_{\Theta} = \tau_{\Theta}/T = 0.33$. For a pair of filaments that reverse immediately after a decrease in overlap is detected (strong thigmotaxis, the response time $\tau \approx 0$), this value corresponds to filaments reversing after losing contact over approximately a single cell (bead).

Finally, each filament's global, overlap-independent reversal rate is set by allowing each filament to reverse after an exponentially distributed time with the mean $\tau_{\mathrm{random}} = 5$ min, that is, after the time it takes a filament to travel its length on a substrate in line with our experiments. In simulations, we thus set $\tau'_{\mathrm{random}} = \tau_{\mathrm{random}}/T = 20$.

The measurement of the response time τ of smart reversals from experiments is described in detail in Section VI.

5. Torques. After encountering and forming rotary bonds in a suspension, filaments are subject to two widespread sources of reorientation: turbulence and drag forces due to settling or rising under gravity. These reorienting effects are represented by the aligning torques [Eq. (S28)], whose magnitude is parameterized by Γ, with units of force. Our choice of Γ is governed by the observation that turbulence-induced reorientation provides the fastest timescale in the aggregation and rearrangement process (**Fig. S7C**).

Individual small elongated filaments suspended in turbulence reorient according to the Jeffrey equation (*75*). The timescale of these reorienting effects is governed by turbulent shear, which at small scales is given by the inverse of the Kolmogorov timescale $\sqrt{\varepsilon/\nu}$, where ε is the turbulence intensity, and ν is the kinematic viscosity of water. Taking $\nu = 10^{-6}\,\mathrm{m^2 s^{-1}}$ and the turbulence intensity characteristic of the ocean surface layer $\varepsilon = 10^{-6}\,\mathrm{W kg^{-1}}$, the magnitude of turbulent shear is 1 $\mathrm{s^{-1}}$. Individual filaments are thus reoriented on a timescale of the order of seconds. Assuming that a pair of filaments constrained by a rotary bond reorients on a similar timescale, we expect a pair of filaments to align within seconds. Once aligned, stickiness forces prevent further relative rotations between filaments.

Even under quiescent conditions, a pair of buoyant filaments constrained by a rotary bond but otherwise randomly oriented will randomly realign. This reorientation results from different drag forces due to their random orientations that, in turn, induce relative torque between the filaments. We roughly estimate this realignment timescale as the time it would take two randomly oriented filaments to separate if the bond did not connect them spatially: buoyant millimetric filaments with a density offset of about 10% of that of water will sink or rise at speeds of the order of tens of microns per second, traveling a distance equal to their body length within tens of seconds. Assuming that for filaments constrained by a rotary bond, the hydrodynamic interactions do not affect the hydrodynamic drags by more than an order of magnitude as compared to the case of independent filaments, the filaments are thus expected to align within tens of seconds.

External (turbulence-induced) torques will thus reorient and align a pair of filaments within seconds. This timescale is much faster than the tens of minutes needed for a filament to glide its body length, or the encounter timescale, which is on the order of many hours or longer (**Fig. S7**) (*43*). In simulations, we thus set $\Gamma' = \Gamma/\gamma/(LT^{-1}) = 40$. This choice then gives the total reorienting force of $2\Gamma' = 80$, whereas the total propulsive force for a filament in full overlap with a surface is of the order of $(N+1)f = 20$. Thus, in simulations, a pair of filaments aligns roughly four times more rapidly than it takes the filaments to glide their body lengths, respecting the direction of the separation of timescales (**Fig. S7C**).

B. Simulation parameters

1. Simulations in 2D. In **Fig. 2H**, we studied a simplified variant of the 2D bead-spring model of smart reversals to demonstrate that changing the reversal frequency upon contact results in a uniform distribution of Lack-of-overlap values, rather than the skewed distribution we observed in *Trichodesmium* populations. The filament parameters were as listed in **Table S3** with two changes. First, no smart reversals were present, that is $\tau = \infty$. Second, filaments doubled their random reversal frequency by changing $\tau'_{\mathrm{random}} = 20$ to τ'_{random} =10 upon contact with another filament. We performed 32 simulations with 30 filaments on a square domain of size $L'_{\mathrm{box}} = L_{\mathrm{box}}/L = 150$, each of simulation length $T'_{\mathrm{sim}} = T_{\mathrm{sim}}/T = 1000$. In these simulations, we identified all instances of pairs of aligned filaments and measured their Lack-of-overlap value; the corresponding population distribution is shown in **Fig. 2H** (thick orange line). As an alignment criterion, we required that the angle between the filaments is smaller than 5°.

For the full model with smart reversals, in **Fig. 3A** and in **Movie S11** we show a single simulation with 100 strongly thigmotactic filaments on a domain of size $L'_{\mathrm{box}} = L_{\mathrm{box}}/L = 300$, run for $T'_{\mathrm{sim}} = T_{\mathrm{sim}}/T = 2000$. Filament parameters were as listed in **Table S3** with $\tau = 0.05$.

In **Figs. 3B, C**, at least six runs were performed for each thigmotaxis level (parameters as in **Table S3**). In each run, there were 20 filaments on a domain of size $L'_{\mathrm{box}} = L_{\mathrm{box}}/L = 120$ (or =

100), with simulation length $T'_{\text{sim}} = T_{\text{sim}}/T = 500$. The Lack-of-overlap histograms in **Fig. 3C** were obtained as described above for **Fig. 2H**.

2. Simulations in 3D. To model random encounters by sequential arrivals of individual filaments onto a growing aggregate in three dimensions (**Fig. 3D, E**), we set $D' = D/(L^2/T) = 300$ in Eq. (S27) and use a cubic domain of size $L'_{\text{box}} = L_{\text{box}}/L = 200$, ten times greater than the length of an individual filament. With ten filaments in the domain, this parameter choice gives the initial encounter timescale comparable with the time of a filament to glide its body length. As filaments attach to form the growing aggregate and are thus depleted from the bulk, the encounter timescale increases with the growing aggregate, and when the last filament remains to be collected, the encounter timescale is several-fold greater than the time to glide one body length. Thus, our parameter choice of (D, L_{box}) is motivated by the trade-off between keeping the lengths of the simulations short enough for computational feasibility while respecting the separation of timescales of the aggregation process (**Fig. S7C**). The simulation run time was $T'_{\text{sim}} = T_{\text{sim}}/T = 1000$. The filament parameters were as listed in **Table S3** for the thigmotactic case (blue curve in **Fig. 3D**, **E**; **Movies S12** and **S15**). For the other cases (random reversals, rigid bonds, rotational bonds, etc. in **Fig. 3D**; **Movies S13** and **S14**) the corresponding features of the model were switched off, as discussed in the Main Text.

3. Time stepping. In all simulations, we used the forward Euler scheme. The time step was in the range $\Delta t/T = 10^{-8} - 10^{-5}$. We typically divided simulations into pieces (usually 100 or more), and some pieces had smaller time steps than others whenever resolving collisions between filaments was necessary.

X. Coagulation model of aggregation in the ocean

Two mechanisms may constitute a source of new filaments in a growing *Trichodesmium* aggregate in the ocean: growth or encounters between filaments. Under bloom conditions, with *Trichodesmium* concentration reaching 10^7 filamentsm^{-3}, the encounter timescale between individual filaments can be below one day for a broad range of environmental conditions representative of the ocean surface layer (*43*). As mentioned in the Main Text, this encounter timescale is significantly shorter than *Trichodesmium*'s doubling time of a few days, suggesting that encounters may easily outcompete growth in forming aggregates under bloom conditions. Previous field observations also reported the presence of aggregates at lower filament concentrations ($10^5 - 10^6$ filaments m^{-3}, including individual filaments and filaments in aggregates), but only free filaments with few or no aggregates were present at even lower concentrations (*6*). The absence of aggregates at low concentrations and their emergence at higher concentrations is consistent with encounter-driven aggregation. In contrast, it would be less clear why the proportion of individual filaments vs. filaments in aggregates should depend on the overall concentration of filaments if aggregates are formed by growth only. Based on these observations, we suggest as plausible that growth may act primarily as the source of individual filaments in the water column until the concentration of individual filaments is high enough for encounters to drive aggregation.

Here, we make the above argument quantitative by analyzing how fast encounters can convert an environmentally relevant concentration of individual filaments into aggregates. We study Smoluchowski coagulation equations that represent the time evolution of the mean concentrations of individual filaments and their aggregates that form upon encounters (**Fig. S7A**). Specifically, following Słomka and Stocker (*66*), we simulate the following equations

$$dc_i/dt = -c_i \sum_{j=1}^{N} \Gamma_{ij} c_j + \frac{1}{2} \sum_{j}^{i-1} \Gamma_{ji-j} c_j c_{i-j} \,, \tag{S30}$$

where c_i represents the concentration of i-bundles, that is, bundle-like aggregates containing i individual filaments, and Γ_{ij} is the encounter kernel between bundles containing i and j filaments. As in reference (*66*), an i-bundle is a cylinder of length l and aspect ratio $Ai^{-1/2}$ and volume $V_i = \pi l^3/(4A_i^2)$. We assume that the encounters between aggregates are induced by two mechanisms: settling due to the density offset $\Delta\rho$ and turbulence characterized by the intensity ε. Accordingly, for collision kernels, we take

$$\Gamma_{ij} = \Gamma_{ij}^{\text{rods}} + \Gamma_{ij}^{\text{turb}} \,, \tag{S31}$$

where $\Gamma_{ij}^{\text{rods}}$ describes encounters induced by sinking and is described in detail in (*66*). For the turbulence-induced encounters, we consider two cases: encounters between identical bundles ($i = j$) and encounters between dissimilar bundles ($i \neq j$). For encounters between identical bundles, we use the recently derived kernel describing encounters between identical elongated filaments (*43*). For dissimilar bundles, we take a conservative approach and assume that bundles collide with the same frequency as equal-volume spheres (*67*), in which case $\Gamma_{ij}^{\text{turb}} = 1.3(r_i + r_j)^3\sqrt{\varepsilon/\nu}$, where r_i is the radius of a sphere with volume V_i. In simulations, we use the following representative parameters: $l = 1$ mm, $A = 100$, $\Delta\rho = 50$ kgm^{-3}, $\varepsilon = 10^{-6}$ Wkg^{-1}, $\nu = 10^{-6}$ m^2 s^{-1}.

Note that in Eq. (S31), we explicitly do not include growth terms to study the speed at which collisions alone convert individual filaments into bundles of filaments. For initial conditions, we use $c_1 = 10^6\ \mathrm{m}^{-3}$ and all other concentrations $c_i = 0$, representing initial conditions corresponding to a suspension of individual filaments and no aggregates.

We note that the coagulation model differs from the bead-spring model (Sections V and VIII) in several ways. The coagulation model is a mean-field model; it only represents mean concentrations of aggregates of different sizes as a function of time, whereas the bead-spring model explicitly resolves individual filaments, their positions, and thigmotactic behavior. Thigmotactic activity in the coagulation model is implicitly represented by the rule that an encounter between two bundle-like aggregates leads to forming of another, thicker bundle-like aggregate. This is justified by the separation of timescales between the time it takes for filaments to align and rearrange upon encounter (minutes and tens of minutes) and the encounter timescale (hours to days). We used the bead-spring model to study the formation of an individual aggregate over several hours from a single seed aggregate driven by encounters represented as an effective diffusion. By contrast, by not explicitly resolving the position and behavior of individual filaments but only representing mean concentrations, the coagulation model allows us to scale up and consider hundreds of aggregates of different sizes forming over many days.

The results of the coagulation dynamics are shown in **Fig. S7B**. We find that starting with million individual filaments per cubic meter, 90% of initial individual filaments are incorporated into some aggregate [$i > 1$ in Eq. (S30)] within less than eight days. After about five days, thousands of aggregates per cubic meter emerge, each containing ten filaments ($i = 10$). After about nine days, driven by further encounters, tens of aggregates per cubic meter emerge, each containing a hundred filaments ($i = 100$). By contrast, for a single filament to grow and form an aggregate containing a hundred filaments, the filament has to undergo about seven division cycles. Assuming the typical doubling time of three days under favorable conditions (*4*), and assuming that no filaments are lost from the aggregate during each division cycle, it would take a single filament about three weeks to grow into a sizable aggregate.

Finally, we estimate the typical hydrodynamic shear forces that turbulence may exert on a pair of filaments that adhere to each other. The integral of shear stress over the filament surface gives shear forces on a filament immersed in water. We estimate the magnitude of turbulent shear stress by the product of the dynamic viscosity of water (μ =1 mPa s) and turbulent shear rate, which is given by $\sqrt{\varepsilon/\nu}$, the inverse of the Kolmogorov timescale. Taking the turbulence intensity characteristic of the ocean surface layer $\varepsilon = 10^{-6}\ \mathrm{Wkg}^{-1}$, the kinematic viscosity of water $\nu = 10^{-6}\ \mathrm{m}^2\ \mathrm{s}^{-1}$, and the filament dimensions to be that of a cylinder of radius $r = 5$ μm and length $l = 1$ mm (surface area $\sim 2\pi rl$), we obtain the shear forces in the range $\mu \sqrt{\varepsilon/\nu}\ (2\pi rl)$ ~ 30 pN. Previous atomic force microscopy measurements of filament stickiness indicate adhesive forces in the range of tens of nanoNewtons (*12*), three orders of magnitude larger than the forces induced by turbulence. Consequently, provided that filaments are sticky, turbulent shear forces are unlikely to separate a pair of filaments that stick to each other in the open ocean.

XI. Comparison with aggregation in other active matter systems.

Active matter systems are composed of self-driven active particles, each capable of systematic movement (*52, 53*). An example is *Myxococcus xanthus*, a rod-shaped, soil-dwelling bacterium that uses gliding to form multicellular fruiting bodies on surfaces (*54*). The formation of fruiting bodies in *Myxococcus xanthus* has been rationalized as resulting from cell jamming driven by high cell densities, gliding, and reversals (*54*), a form of phase separation called motility-induced phase separation (*76*). Specifically, wild-type cells speed up and suppress reversals upon starvation, inducing phase separation and formation of fruiting bodies. *Pseudomonas aeruginosa,* an opportunistic rod-shaped pathogen*,* can avoid such jamming on surfaces by triggering reversals upon contact, a form of mechanotaxis (*55*). Such mechanotaxis, guided by mechanical input from type IV pili, enables *Pseudomonas* to colonize surfaces uniformly at high cell densities. *Trichodesmium* aggregation is different: in the three-dimensional habitat of the open ocean, the concentrations of these organisms are too low to produce filament jamming. Even under bloom conditions, where concentrations can reach 10^7 filaments m^{-3} (*44*), suspended filaments are typically separated by a distance about ten-fold larger than the filament length. Instead, *Trichodesmium* uses smart reversals to convert encounters into aggregates.

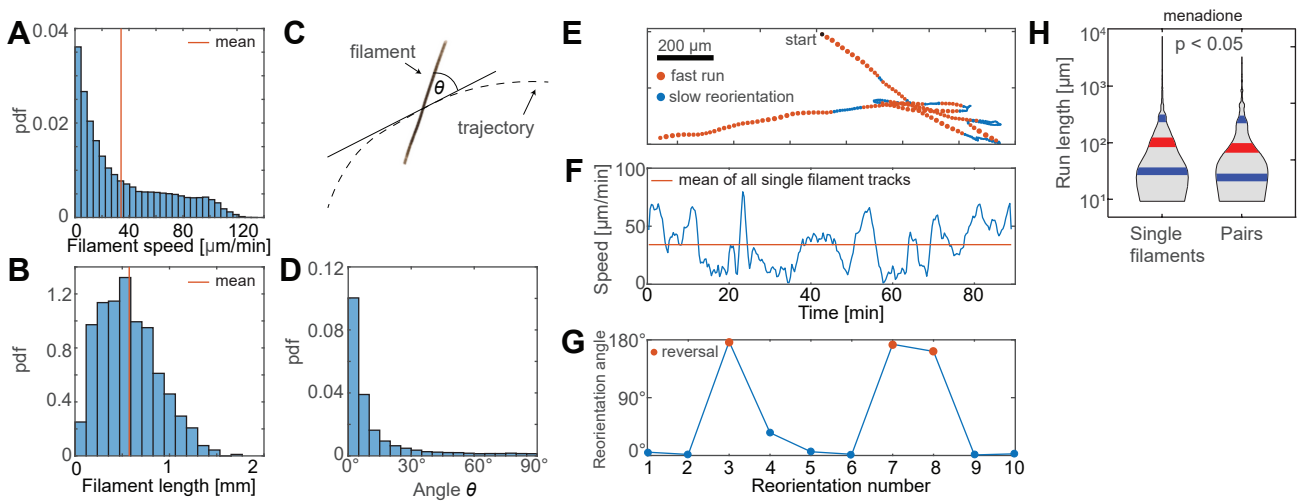

Fig. S1 | Illustration of the analysis of filament tracks. In **A-G** shown is the combined data from 12 experiments on non-aggregating (exponentially growing) control cultures; tracks from aggregating (menadione-induced) cultures were analyzed analogously. **A,** The distribution of instantaneous filament speeds from all individual tracks (34.1 ± 31.9 µm min^{-1}, mean ± sd, n = 776 tracks). **B,** The distribution of individual filament lengths (0.57 ± 0.31 mm, mean ± sd, n = 776 filaments). **C**, To quantify the gliding direction of a filament, we measured the angle θ between the filament's long axis and the tangent to the trajectory of the centroid of the filament. **D**, The histogram of θ in an ensemble of single filaments tracks (n = 776 tracks) shows that filaments glide primarily along their long axis. **E,** Segmentation of a single filament track into runs and reorientations. **F**, Runs and reorientations are defined by the corresponding instantaneous filament speed being larger or smaller than the mean of all single filament tracks (**A**). **G**, The reorientation angle is defined as the angle between the tangent vectors to the trajectory at the end of a run and the start of the subsequent run. A reversal is defined as a reorientation event with a reorientation angle greater than 90°. In **A**, **B**, and **D**, the data set is the same as in **Fig. 2B, C** (non-aggregating control culture). The example in **E-G** is the same as in **Fig. 2A**. **H**, Violin plot (the grey area) comparing raw (i.e., not normalized by filament length) run lengths in menadione for single filaments and filaments in pairs. The red line shows the median, and the blue lines show the 25th and 75th percentiles. The data is the same as in **Fig. 2E**, except for the normalization. The statistical test on the raw run lengths is the Kolmogorov-Smirnov two-sample one-sided test (n_{single} = 1964, n_{pairs} = 377; test statistic k = 0.0731). See **Tables S1 and S2** for a summary of gliding motility statistics.

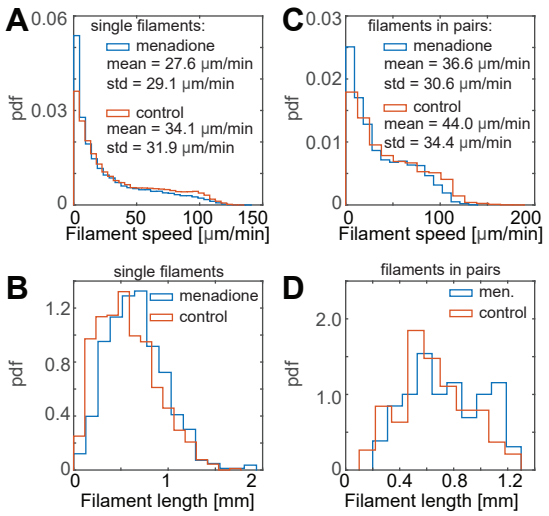

Fig. S2 | Speed and length distributions of single filaments (**A**, **B**) and filaments in pairs (**C**, **D**) for both menadione and control. See also **Table S1**.

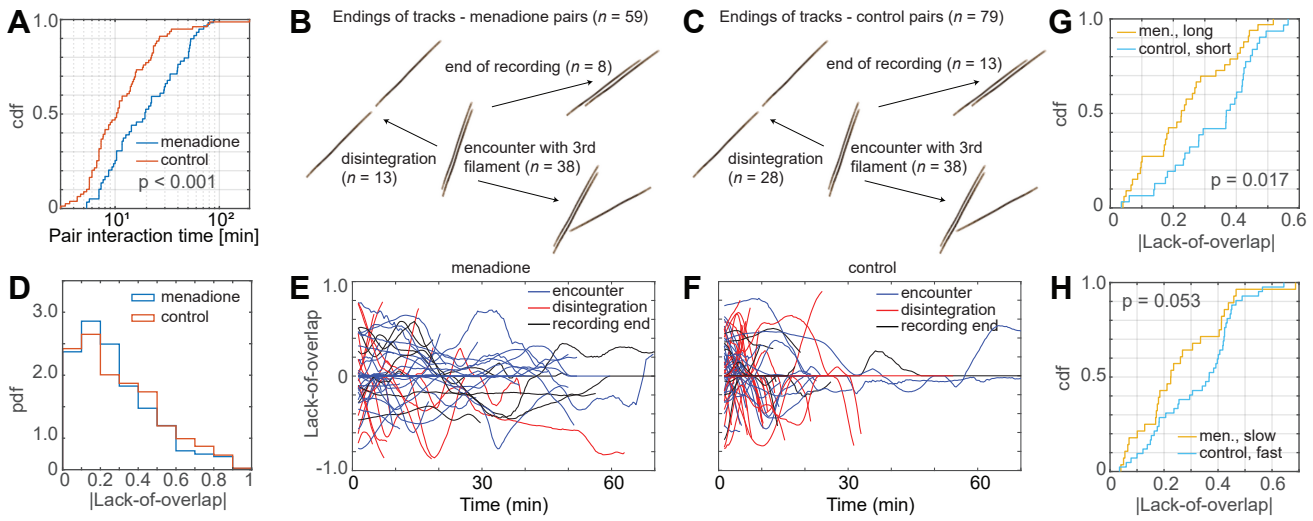

Fig. S3 | Additional analysis of smart reversals and disintegration rates of pairs of filaments in menadione and control. A, The cumulative distribution function of the interaction time (track duration) of pairs of filaments for both menadione-treated cultures and control cultures shows that pairs of filaments in the control spend less time together than pairs of filaments in menadione (16.8 min ± 24.4 min vs. 26.7 min ± 20.8 min; mean ± std; $n_C = 79$, $n_M = 59$). The p value was obtained from the two-sample one-sided Kolmogorov-Smirnov test (test statistic $k = 0.3182$). **B**, **C**, The three possible ways in which the track of a filament pair ends in our experiments for both menadione-treated cultures (**B**) and control cultures (**C**). Combining the pair interaction time (**A**) with the statistics of the track endings (**B**, **C**), shows that filament pairs disintegrate 2.5-fold more rapidly in the control than in menadione (**Supplementary Text Section IV**). **D**, The histogram of the Lack-of-overlap (non-zero values) for all tracks is more skewed towards small values for menadione than for the control (mean 0.28 vs. 0.30 and skewness 0.96 vs. 0.75, respectively), implying a stronger smart reversal response for menadione. This difference is, however, not statistically significant. **E**, **F,** The corresponding time series of the Lack-of-overlap for both menadione-treated cultures (**E**) and control cultures (**F**). **G**, Cumulative distribution function of the Lack-of-overlap shows that the Lack-of-overlap is more skewed towards small values for long filaments (>600 μm) in menadione than for short filaments (< 600 μm) in the control. **H**, Similarly, the cumulative distribution function of the Lack-of-overlap shows that the Lack-of-overlap is more skewed towards small values for slow (< 40.3 μm min^{-1}) filaments in menadione than for fast (> 40.3 μm min^{-1}) filaments in the control. The distributions in (**G**) and (**H**) corroborate the idea that slower or longer filaments perform smart reversals more efficiently (i.e., have a lower probability of failing to reverse) than faster or shorter ones (**Supplementary Text Section VII; Table S2**). The p values in (**G**) and (**H**) were obtained from the two-sample one-sided Kolmogorov-Smirnov test (test statistic $k = 0.3441$, $n_C = 31$, $n_M = 33$, in **G**; $k = 0.2857$, $n_C = 42$, $n_M = 28$, in **H**). Each track contributes one point in (**G**) and (**H**) by averaging the absolute non-zero value of the Lack-of-overlap over the track.

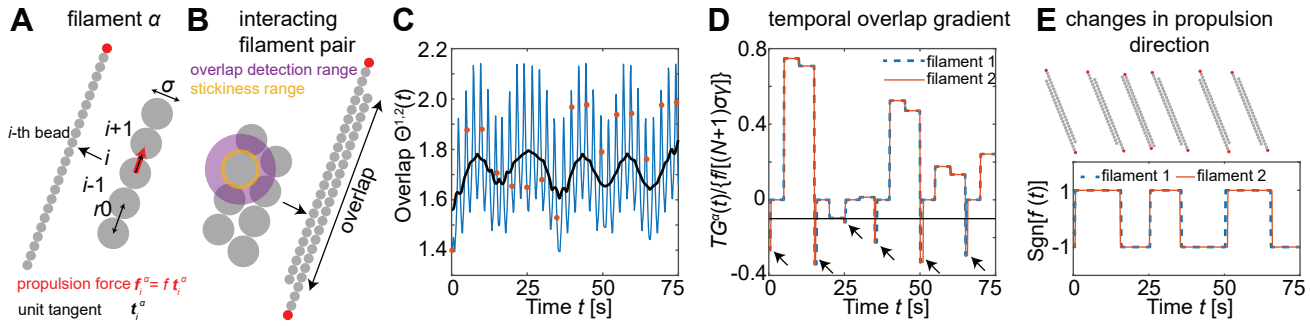

Fig. S4 | The bead–spring model of thigmotactic filaments on a substrate. A, In the model, each filament is treated as an inextensible, semi-flexible chain composed of 20 beads, representing *Trichodesmium* cells, capable of elastic (inextensibility) and bending (semi-flexibility) interactions (**Supplementary Text Section V**). Each bead can generate a propulsion force of fixed strength oriented along the filament's long axis (red arrow), which can produce traction by pushing against the substrate or other filaments (**Supplementary Text Section V.A**). The directions of the propulsion forces at any moment on a given filament are all the same and are indicated by the red bead. These directions can all reverse simultaneously due to either thigmotactic behavior (overlap-induced reversals) or randomly (overlap-independent reversals; **Supplementary Text Section V.B**). **B**, When in contact, filaments interact through truncated Lennard-Jones steric repulsion and stickiness [the ranges of single-bead repulsion and attraction are shown in grey and yellow, respectively; (**Supplementary Text Section V.A**)] and can pull on each other when sufficiently aligned (forces not shown). Furthermore, filaments sense their mutual overlap with other filaments by averaging the overlap of individual beads along the filament length (**Supplementary Text Section V.B**). The overlap (coordination number) of a single bead is defined through an effective Lennard-Jones potential (range shown in purple; **Supplementary Text Section V.B**). **C-E**, Behavior of two strongly thigmotactic filaments after a random encounter on a substrate - the filaments form a dynamic oscillatory bound state by reversing their direction of gliding when they detect a temporal decrease in their overlap. **C**, The temporal signal of the mutual overlap between the filaments is shown in blue; the black curve shows the trend (moving average). The high-frequency modulation of the blue signal is the result of integrating the overlap signal over a finite number of equally spaced sensors (beads). The red points represent the time instances, spaced equally every τ_Θ, at which the filaments sample the continuous signal (**Fig. S9**). **D**, The temporal gradient in overlap as estimated by each filament (**Supplementary Text Section V.B**). When the gradient is sufficiently negative (black line at -0.1; **Supplementary Text Section V.B**), the filaments reverse their direction of motion (arrows represent the moment of reversal) after an exponentially distributed time, in this case with mean $\tau = 0.75$ s (the lag time, with this case representing strong thigmotaxis). **E**, Reversals represented by the periodic changes in the directions of the propulsive forces and the corresponding snapshots of filament arrangement just before each reversal.

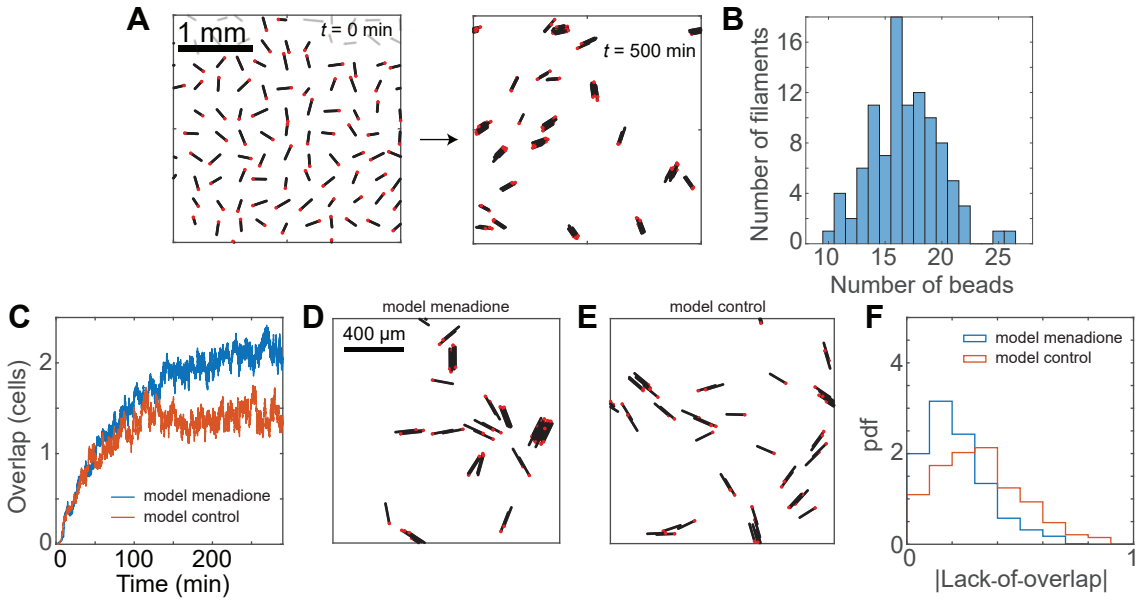

Fig. S5 | Additional simulations of filaments gliding and aggregating on a surface. A, B, Results of a simulation of strongly thigmotactic filaments show that filament length variability does not prevent aggregation. All the parameters are the same as in **Fig. 3A**, except for the lengths of filaments. Here, we assumed that each filament was composed of a number of cells (beads) sampled from a Gaussian distribution with a mean of 17 and standard deviation of 3, rounded to an integer value (in **Fig. 3A,** all filaments were composed of 20 beads). The histogram in (**B**) shows the resulting distribution of the number of beads per filament used in the simulation. **C-F**, Additional model simulations in 2D on a surface with parameters mimicking the menadione and control conditions of the experiments (**Supplementary Text Section VI**). The control filaments are 20% faster, 10% shorter, and have an 80% longer response time than menadione filaments, as in the experiments (**Table S1**). Both model conditions have a skewed Lack-of-overlap (**F**) because they perform smart reversals. Still, the control condition reaches an overall lower overlap level (i.e., lower level of aggregation) since it forms transient aggregates that disintegrate more frequently.

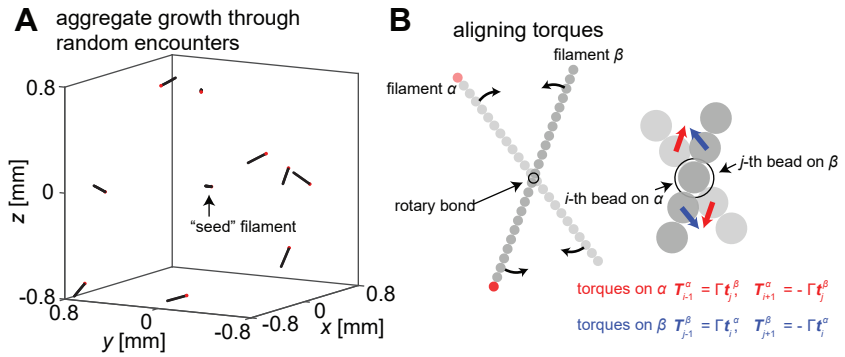

Fig. S6 | Bead–spring model of the formation of an aggregate in 3D by sequential, random arrivals of randomly oriented filaments onto a seed filament. A, We model random encounters in 3D as an effective diffusion process (**Supplementary Text Section VIII**). For initial conditions, we distribute ten filaments at random positions and orientations in a cubic domain with sides of length ten times greater than the filament length. We then focus on a single 'seed' filament that performs a random walk and collects other filaments; members of such a growing aggregate diffuse together while other filaments remain stationary. In simulations, we work in the frame of the growing aggregate so that the aggregate remains stationary and all other filaments move according to the same random walk. Filaments that come into contact through this encounter process experience effective external torques and perform thigmotaxis upon alignment (**Supplementary Text Section VIII**). **B**, For any pair of filaments in contact, a rotational bond is formed between one bead from each filament (**Supplementary Text Section VIII**). The aligning torques, such as those generated by turbulence, are realized by forces that act on the nearest neighbors of the beads forming the bond. These forces act along directions tangential to the two filaments, which leads to their alignment.

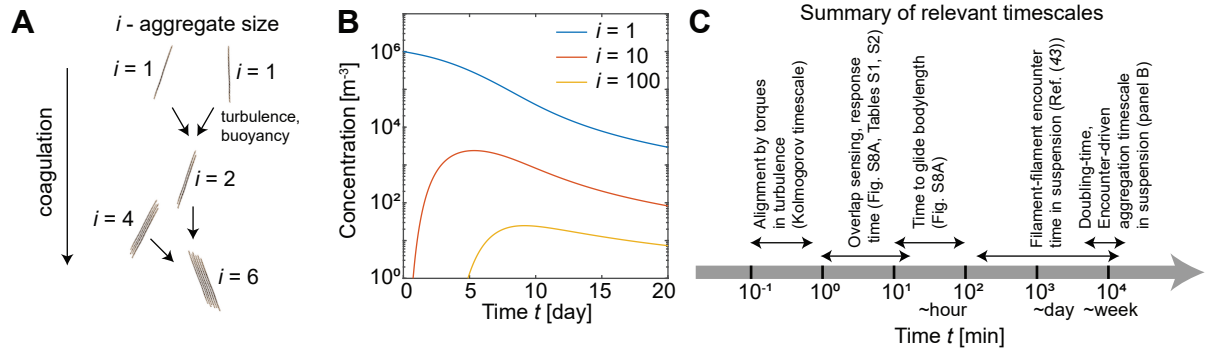

Fig. S7 | Timescales of aggregation. A, To estimate the timescale of encounter-driven aggregation in the ocean from a suspension of individual filaments, we simulate a coagulation model of filaments encountering each other under the action of turbulence and buoyancy and forming tight aggregates as a result of their alignment and thigmotaxis (**Supplementary Text Section X**). The coagulation model is different from the bead–spring model (**Fig. S4-6**) in that it represents mean concentrations of aggregates of different sizes and does not resolve the positions and behavior of individual filaments in a single aggregate, which allows modeling of the formation of many aggregates over much longer aggregation timescales. In the coagulation model, thigmotactic activity is implicitly represented by the rule that encounters between different aggregates result in the formation of tight bundles (**Supplementary Text Section X**). **B**, Results of simulation of the coagulation model for an initial concentration of individual filaments (i = 1) equal to 10^6 m^{-3} and no aggregates show that aggregates composed of ten (i = 10) and one hundred (i = 100) filaments emerge after several days and that 90% of individual filaments are incorporated into some aggregate within eight days (**Supplementary Text Section X**). By contrast, given that the doubling time of *Trichodesmium* under favorable conditions is about three days, it would take several weeks to form aggregates by growth only (**Supplementary Text Section X**). **C**, Summary of the relevant timescales of *Trichodesmium* encounter in the ocean and subsequent rearrangement into aggregates. The lower range of the filament-filament encounter timescale corresponds to conditions of strong turbulence ($\varepsilon = 10^{-4}$ Wkg^{-1}) and filament concentration representative of bloom conditions (10^7 m^{-3}), whereas the upper range corresponds to moderate turbulence ($\varepsilon = 10^{-6}$ Wkg^{-1}) and filament concentration representative of non-bloom conditions (10^6 m^{-3}). The encounter-driven aggregation timescale corresponds to the simulation in (**B**), which was computed for moderate turbulence ($\varepsilon = 10^{-6}$ Wkg^{-1}) (**Supplementary Text Section X**).

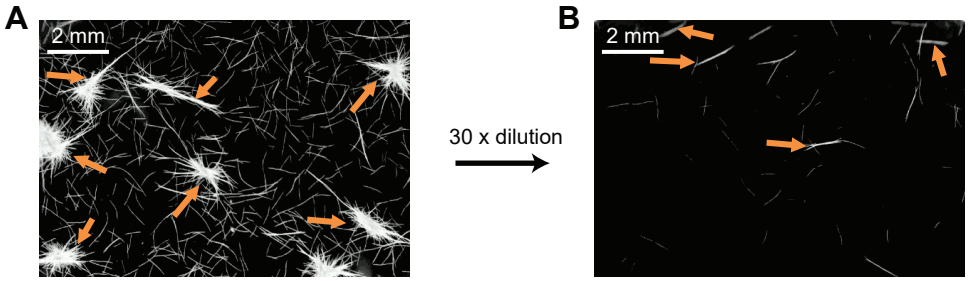

Fig. S8 | Puffs emerge at high filament densities. A, In our aggregation experiments, a variety of aggregate shapes emerged at high filament densities (71.2 filaments/mm^2), including puff- and tuft-like arrangements. **B**, After 30× dilution of the same cultures (2.4 filaments/mm^2), tight bundles (tufts) dominated, and puff-like aggregates only formed upon encounters among bundles. Panel (**A**) is the same as in **Fig. 2D**.

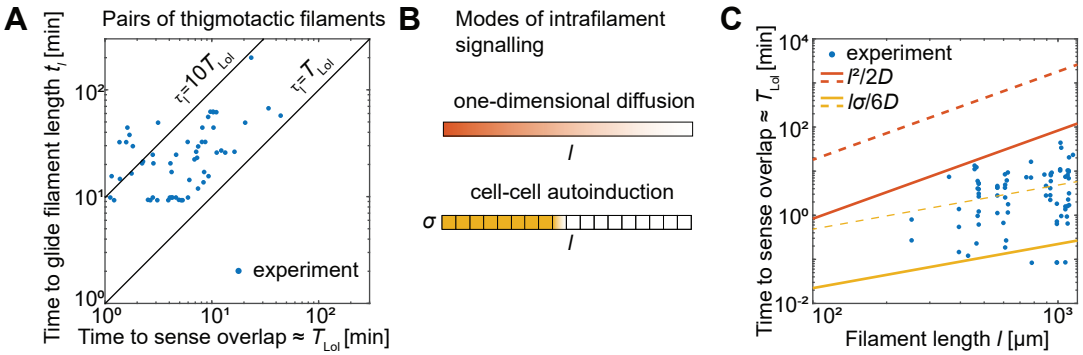

Fig. S9 | Sensing timescales and potential intrafilament signaling mechanisms. **A**, Comparison of the time needed to glide a distance equal to the filament length and to sense overlap in pairs of thigmotactic filaments observed in the menadione-induced cultures. As a proxy for the sensing time, we use the time T_{LoI} needed for a filament in a pair to glide, at its mean speed, a distance corresponding to the value of the Lack-of-overlap at the instance of reversal. Each dot represents a single reversal event in (n = 59) pairs (same dataset as in **Fig. 2E**). **B**, Two potential modes of intrafilament signaling by a signaling molecule or protein with diffusion constant D in a filament of length l composed of cells of size σ: simple one-dimensional diffusion (signaling time scales as $l^2/2D$) or autoinduction, in which each cell amplifies the signal (signaling time scales as $l\sigma/6D$) (**Supplementary Text VI.A**). Adjusting the concentration threshold of the response to the propagating signal could delay the onset of a reversal and thus modulate the thigmotaxis level. **C**, The proxy for the sensing time (same as in **A**) as a function of the filament length falls between the two scaling regimes. The two scaling regimes are shown for a small signaling molecule with diffusion constant D = 100 μm^2 s^{-1} and a signaling protein with D = 4.6 μm^2 s^{-1} (broken line) for cell size σ = 8 μm. The sensing timescale also served as a proxy for the time interval τ_Θ at which filaments in the model sample overlap (**Fig. S4C**; **Supplementary Text V.B**).

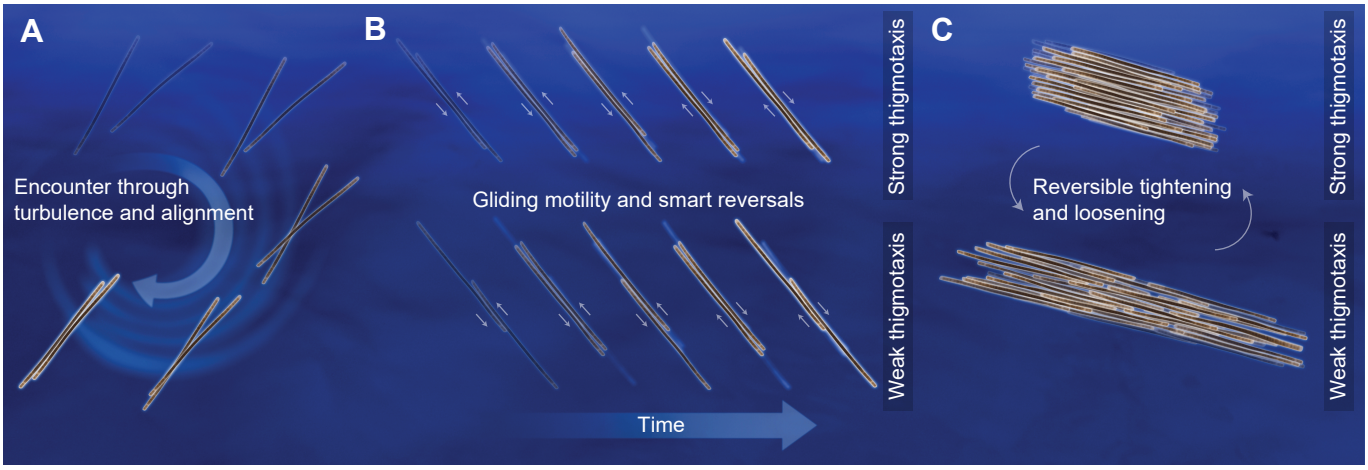

Fig. S10 | Schematic of the mechanisms controlling *Trichodesmium* aggregate formation and reshaping. A, Filaments in the ocean are sparse and likely encounter each other over many hours through the action of turbulence, which also acts to align them. **B**, Gliding motility of filaments on each other, by itself, would rapidly cause nascent aggregates to disintegrate. Instead, thigmotactic behavior allows filaments to stay together and aggregates to grow through additional encounters. Thigmotaxis is realized by smart reversals that occur in response to decreasing overlap between filaments. Thigmotaxis strength is controlled by a single parameter, the response time that controls the delay between sensing a decrease in overlap and reversing. **C**, Within an aggregate, filaments can control aggregate architecture in response to environmental conditions by modulating the strength of their thigmotaxis, thereby loosening or tightening the aggregate.

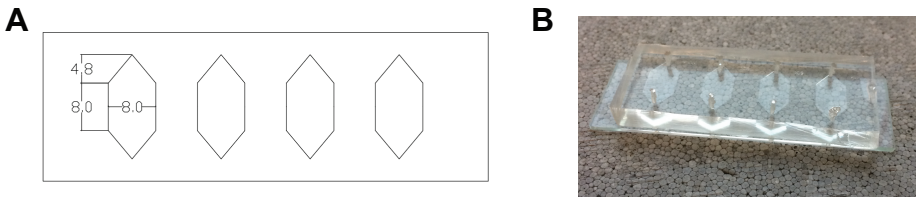

Fig. S11 | A, Design of microfluidics chambers for observation and quantification of single filament motility and filament–filament interactions (**Materials and Methods**). Units are given in mm. **B**, Image of fabricated chambers.

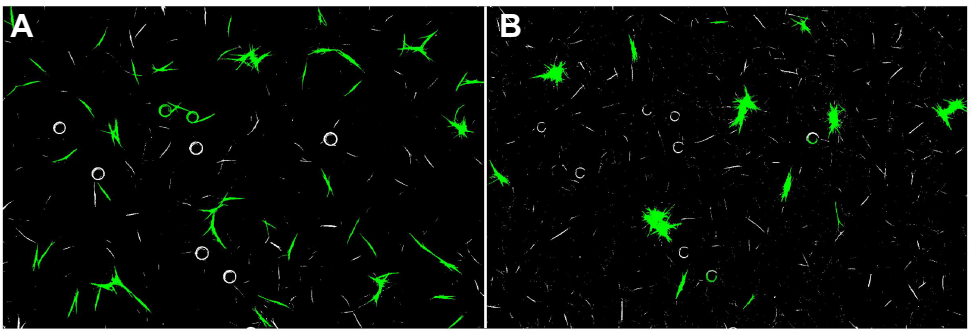

Fig. S12 | Example of the image analysis showing segmentation of images of a stationary phase *T. erythraeum* IMS101 culture, such as used for the experiments characterizing the response of aggregates to changes in light intensity. **A**, An early time point during the formation of aggregates. **B**, A late time point after the formation of tight aggregates. White circles in panel (**A**) are small air bubbles that diminished over the course of the experiment. The segmentation algorithm mostly excluded them.

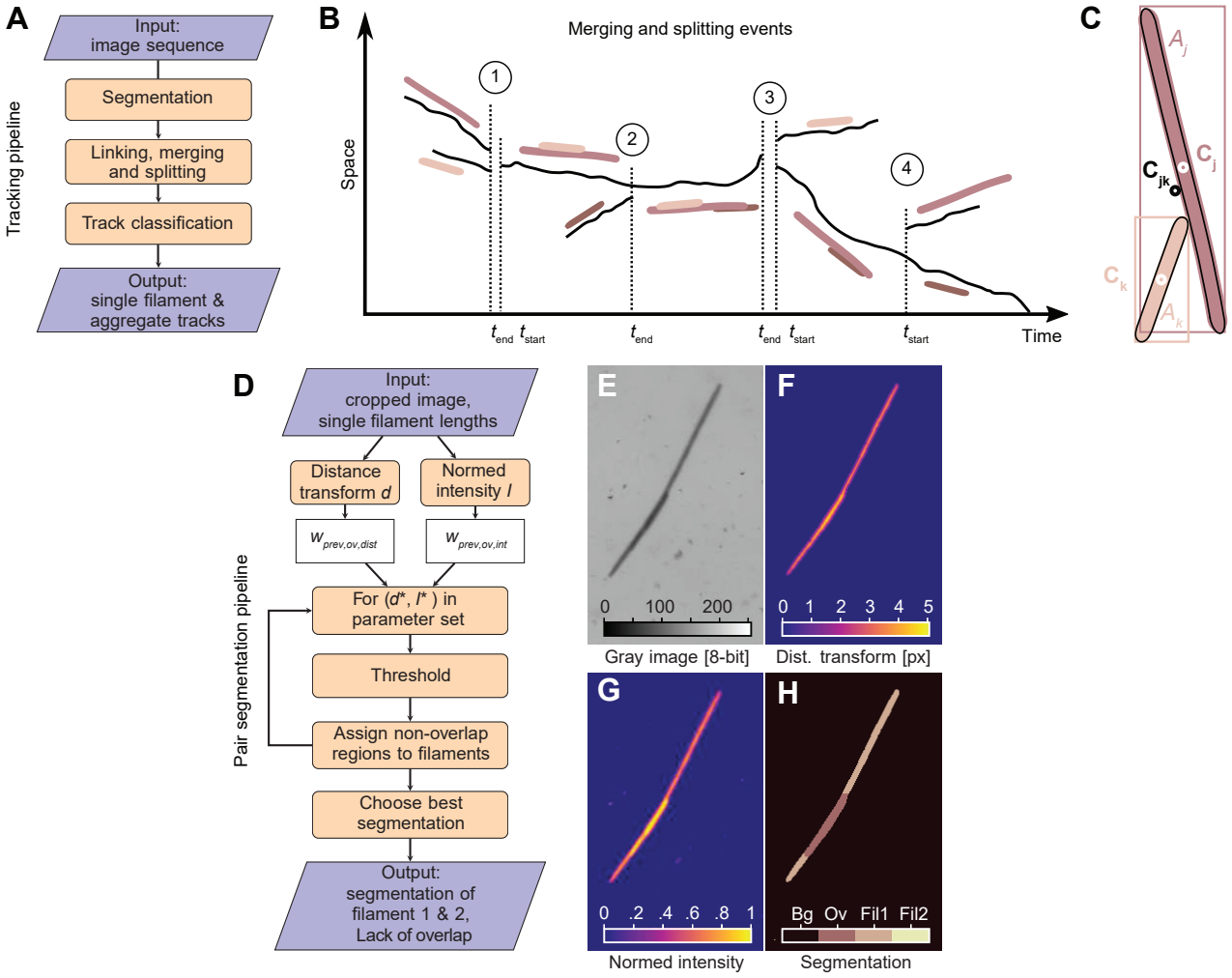

Fig. S13 | Image analysis of filament tracks. A detailed description of the tracking and segmentation pipelines is given in **Supplementary Text Section I**. **A**, Filament tracking pipeline. **B**, Schematic of merging and splitting events of filament tracks (black lines) and interpreted filament behavior (brown images): (1) the ends of two tracks are linked to the start of one track, (2) the end of one track is linked to the middle of another track, (3) the end of one track is linked to the starts of two tracks and (4) the start of one track is linked to the middle of another track. The continuous tracks in (2) and (4) are split into a single filament and an aggregate track. **C**, Calculation of estimated aggregate centroid $\mathbf{C_{jk}}$ of filaments j and k. **D**, Processing pipeline to determine the extent of overlap in a filament pair. **E-H**, Example images of the different stages of the processing pipeline. **H**, The segmented image with background (Bg), overlap region (Ov), filament 1 (Fil1), and filament 2 (Fil2) was used in conjunction with the lengths of Fil1 and Fil2 to find the filaments' positions and Lack-of-overlap.

Quantity	Individual filaments (control)	Individual filaments (menadione-treated)	Pairs of filaments (control)	Pairs of filaments (menadione-treated)
Number of tracks (from 12 experiments)	776	643	158 (from 79 pairs)	118 (from 59 pairs)
Speed [μm min^{-1}] (mean ± sd)	34.1 ± 31.9 (*n* = 776)	27.6 ± 29.1 (*n* = 643)	44.0 ± 34.4 (*n* = 158)	36.6 ± 30.6 (*n* = 118)
Length [μm] (mean ± sd)	574 ± 308 (*n* = 776)	664 ± 302 (*n* = 643)	651 ± 258 (*n* = 158)	743 ± 272 (*n* = 118)
Run time [min] (mean ± sd)	5.4 ± 8.2 (*n* = 2146)	5.2 ± 8.2 (*n* = 1964)	3.8 ± 4.1 (*n* = 312)	3.8 ± 5.4 (*n* = 377)
Run length [μm] (mean ± sd)	375 ± 708 (*n* = 2146)	312 ± 650 (*n* = 1964)	276 ± 380 (*n* = 312)	239 ± 418 (*n* = 377)
Run length/filament length (mean ± sd)	0.88 ± 1.97 (*n* = 2146)	0.63 ± 1.52 (*n* = 1964)	0.52 ± 0.78 (*n* = 312)	0.41 ± 0.85 (*n* = 377)
Reversal probability (mean ± sem)	0.43 ± 0.01 (*n* = 1518)	0.38 ± 0.01 (*n* = 1450)	0.53 ± 0.04 (*n* = 169)	0.40 ± 0.03 (*n* = 266)
Fraction of time spent in run mode (weighted mean ± weighted sd)	0.37 ± 0.33 (*n* = 776)	0.35 ± 0.32 (*n* = 643)	0.45 ± 0.29 (*n* = 158)	0.46 ± 0.30 (*n* = 118)
Reversal frequency [min^{-1}] (weighted mean ± weighted sd)	0.020 ± 0.033 (*n* = 776)	0.019 ± 0.030 (*n* = 643)	0.033 ± 0.040 (*n* = 158)	0.034 ± 0.040 (*n* = 118)
Pair interaction time [min] (mean ± sd)	N/A	N/A	16.8 ± 24.4 (*n* = 79)	26.7 ± 20.8 (*n* = 59)
Pair disintegration rate [min^{-1}] (mean ± error)	N/A	N/A	0.0210 ± 0.0047 (*n* = 79)	0.0082 ± 0.0022 (*n* = 59)
Escape probability (mean ± error)	N/A	N/A	0.31 ± 0.08	0.12 ± 0.04
Lack-of-overlap (mean ± sem)			0.30 ± 0.02 (*n* = 79)	0.28 ± 0.03 (*n* = 59)
Response time [min] (mean ± error)	N/A	N/A	3.32 ± 0.28	1.82 ± 0.13
Relative response time (mean ± error)	N/A	N/A	0.22 ± 0.02	0.09 ± 0.01

Table S1 | Summary of the gliding motility statistics for individual filaments and filaments in pairs in control and menadione treatment. The quantities: pair disintegration rate, escape probability, response time, and relative response time are computed from other quantities in the table (**Supplementary Text Sections IV** and **VI**). The corresponding errors were computed by propagating standard errors on the mean using error propagation formulae (see code 'analyze_single_filaments.m' and 'analyze_pairs.m' in DOI: 10.3929/ethz-b-000596515).

Quantity	Pairs of filaments (menadione-treated) short vs. long	Pairs of filaments (control) short vs. long	Pairs of filaments (menadione-treated) slow vs. fast	Pairs of filaments (control) slow vs. fast
Number of tracks (from 12 experiments)	42 (21 pairs) vs. 76 (38 pairs)	72 (36 pairs) vs. 86 (43 pairs)	62 (31 pairs) vs. 56 (28 pairs)	64 (32 pairs) vs. 94 (47 pairs)
Speed [μm min^{-1}] (mean ± sd)	50.4 ± 33.5 (*n* = 42) vs. 28.5 ± 25.5.5 (*n* = 76)	47.7 ± 33.7 (*n* = 72) vs. 42.1 ± 34.7 (*n* = 86)	20.2 ± 18.5 (*n* = 62) vs. 59.2 ± 29.4 (*n* = 56)	23.2 ± 19.9 (*n* = 64) vs. 63.2 ± 33.8 (*n* = 94)
Length [μm] (mean ± sd)	488 ± 138 (*n* = 42) vs. 884 ± 219 (*n* = 76)	478 ± 176 (*n* = 72) vs. 796 ± 225 (*n* = 86)	808 ± 276 (*n* = 62) vs. 672 ± 250 (*n* = 56)	679 ± 283 (*n* = 64) vs. 632 ± 240 (*n* = 94)
Run time [min] (mean ± sd)	5.8 ± 7.7 (*n* = 126) vs. 2.9 ± 3.4 (*n* = 251)	4.0 ± 3.2 (*n* = 119) vs. 3.8 ± 4.6 (*n* = 193)	2.1 ± 2.1 (*n* = 213) vs. 6.1 ± 7.2 (*n* = 164)	2.1 ± 2.1 (*n* = 121) vs. 4.9 ± 4.7 (*n* = 191)
Run length [μm] (mean ± sd)	402 ± 615 (*n* = 126) vs. 158 ± 233 (*n* = 251)	286 ± 282 (*n* = 119) vs. 270 ± 430 (*n* = 193)	97 ± 115 (*n* = 213) vs. 424 ± 570 (*n* = 164)	114 ± 135 (*n* = 121) vs. 379 ± 444 (*n* = 191)
Run length/filament length (mean ± sd)	0.84 ± 1.31 (*n* = 126) vs. 0.19 ± 0.30 (*n* = 251)	0.75 ± 0.89 (*n* = 119) vs. 0.38 ± 0.68 (*n* = 193)	0.13 ± 0.20 (*n* = 213) vs. 0.76 ± 1.18 (*n* = 164)	0.19 ± 0.28 (*n* = 121) vs. 0.73 ± 0.92 (*n* = 191)
Reversal probability (mean ± sem)	0.48 ± 0.05 (*n* = 89) vs. 0.36 ± 0.04 (*n* = 177)	0.57 ± 0.07 (*n* = 54) vs. 0.50 ± 0.05 (*n* = 115)	0.35 ± 0.04 (*n* = 158) vs. 0.48 ± 0.05 (*n* = 108)	0.41 ± 0.06 (*n* = 71) vs. 0.61 ± 0.05 (*n* = 98)
Fraction of time spent in run mode (weighted mean ± weighted sd)	0.63 ± 0.29 (*n* = 42) vs. 0.36 ± 0.26 (*n* = 76)	0.50 ± 0.27 (*n* = 72) vs. 0.42 ± 0.30 (*n* = 86)	0.25 ± 0.19 (*n* = 62) vs. 0.75 ± 0.15 (*n* = 56)	0.20 ± 0.17 (*n* = 64) vs. 0.67 ± 0.16 (*n* = 94)
Reversal frequency [min^{-1}] (weighted mean ± weighted sd)	0.037 ± 0.047 (*n* = 42) vs. 0.032 ± 0.035 (*n* = 76)	0.033 ± 0.042 (*n* = 72) vs. 0.034 ± 0.039 (*n* = 86)	0.030 ± 0.039 (*n* = 62) vs. 0.039 ± 0.041 (*n* = 56)	0.023 ± 0.029 (*n* = 64) vs. 0.043 ± 0.046 (*n* = 94)
Pair interaction time [min] (mean ± sd)	27.8 ± 24.7 (*n* = 21) vs. 26.2 ± 18.6 (*n* = 38)	13.2 ± 9.6 (*n* = 36) vs. 19.9 ± 31.8 (*n* = 43)	29.2 ± 21.2 (*n* = 31) vs. 24.0 ± 20.3 (*n* = 28)	19.8 ± 34.7 (*n* = 32) vs. 14.9 ± 13.9 (*n* = 47)
Pair disintegration rate [min^{-1}] (mean ± error)	0.0137 ± 0.0048 (*n* = 21) vs. 0.0050 ± 0.0022 (*n* = 38)	0.0338 ± 0.0077 (*n* = 36) vs. 0.0140 ± 0.0049 (*n* = 43)	0.0044 ± 0.0022 (*n* = 31) vs. 0.0134 ± 0.0044 (*n* = 28)	0.0095 ± 0.0047 (*n* = 32) vs. 0.0315 ± 0.0066 (*n* = 47)
Escape probability (mean ± error)	0.19 ± 0.08 vs. 0.08 ± 0.04	0.52 ± 0.14 vs. 0.21 ± 0.08	0.07 ± 0.04 vs. 0.17 ± 0.06	0.21 ± 0.11 vs. 0.37 ± 0.09
Lack-of-overlap (mean ± sem)	0.32 ± 0.05 (*n* = 21) vs. 0.25 ± 0.03 (*n* = 38)	0.32 ± 0.04 (*n* = 36) vs. 0.29 ± 0.03 (*n* = 43)	0.28 ± 0.03 (*n* = 31) vs. 0.26 ± 0.04 (*n* = 28)	0.27 ± 0.04 (*n* = 32) vs. 0.32 ± 0.03 (*n* = 47)
Response time [min] (mean ± error)	3.45 ± 0.42 vs. 1.12 ± 0.08	6.02 ± 2.00 vs. 2.38 ± 0.22	0.80 ± 0.06 vs. 3.49 ± 0.33	1.34 ± 0.14 vs. 4.92 ± 0.54
Relative response time (mean ± error)	0.36 ± 0.06 vs. 0.04 ± 0.00	0.60 ± 0.21 vs. 0.13 ± 0.02	0.02 ± 0.00 vs. 0.31 ± 0.04	0.05 ± 0.01 vs. 0.49 ± 0.06

Table S2 | Additional analysis of the gliding motility statistics of filament pairs. The dataset of pair interactions in **Table S1** is here further split into short (< 0.6 mm) and long (> 0.6 mm) filament pairs and slow (< 40.3 μm min^{-1}) and fast (> 40.3 μm min^{-1}) filament pairs. Each filament pair is assigned to the short/long and slow/fast categories based on the mean length and speed of the two filaments in the pair. The split indicates that slower or longer filaments perform stronger thigmotaxis than faster or shorter ones (**Supplementary Text Section VII**).

Parameter	Physical units	Simulation units
Cell size $\boldsymbol{\sigma}$	8 μm	1
Cell-cell distance $\boldsymbol{r_0}$	8 μm	1
Propulsion force $\boldsymbol{f/\gamma}$	32 μm min^{-1}	1
Spring constant $\boldsymbol{k/\gamma}$	33.33 s^{-1}	500
Bending rigidity $\boldsymbol{\kappa/\gamma}$	133.33 s^{-1}	2000
Stickiness strength $\boldsymbol{\epsilon/\gamma}$	4.27 μm^2 s^{-1}	1
Overlap sampling time $\boldsymbol{\tau_\Theta}$	5 s	0.33
Response time $\boldsymbol{\tau}$	0.75 s, 12 s, 75s	0.05, 0.8, 5
Random reversal time $\boldsymbol{\tau_{random}}$	5 min	20
Aligning force (3D only) $\boldsymbol{\Gamma/\gamma}$	1280 μm min^{-1}	40

Table S3 | Summary of the bead-spring model parameters characterizing filaments and their interactions in physical units and the nondimensionalized units used in simulations. The characteristic time and length scales used to convert the physical units to the simulation units are $T = 15$ s and $L = 8$ μm. The three values of the response time τ correspond to strong, intermediate, and weak thigmotaxis.

Movie S1 | Rapid response of aggregated *Trichodemium* culture to dark pulses during the day.

Movie S2 | Rapid response of aggregated *Trichodemium* culture to light pulses at night.

Movie S3 | A UV-killed control culture did not form aggregates. Left: aggregating culture. Right: same culture treated with UV.

Movie S4 | Tufts merging into puffs and a puff disintegrating into tufts – examples from Movies S1 and S2.

Movie S5 | *Trichodesmium* filaments gliding in a microfluidic chamber on a glass surface

Movie S6 | *Trichodesmium* filaments gliding on each other on a glass surface

Movie S7 | Micropipette experiment. Suspended *Trichodesmium* filaments can glide on each other away from surfaces.

Movie S8 | *Trichodesmium* filaments from a non-aggregating exponential culture gliding in a microfluidic chamber on a glass surface.

Movie S9 | *Trichodesmium* filaments can reverse gliding direction.

Movie S10 | Menadione-induced (3 μM) aggregation of *Trichodesmium* filaments. Top row: dense cultures. Bottom row: 30x dilution.

Movie S11 | Agent-based model of *Trichodesmium* filaments recapitulates the role of smart reversals in aggregation on surfaces.

Movie S12 | Modeling aggregation in 3D from random encounters: motile filaments with smart reversals form compact bundles.

Movie S13 | Modeling aggregation in 3D from random encounters: sticky filaments with rigid bonds form fractal-like morphologies.

Movie S14| Modeling aggregation in 3D from random encounters: sticky filaments with rotational bonds form elongated chains.

Movie S15 | Modeling tightening and loosening of aggregates in 3D: mimicking light ON/OFF cycles by decreasing/increasing reversal response time.

Movie S16 | Tightening and loosening of a tuft upon Light ON/OFF switches – example from Movie S1.